Accounting for uncertain 3-D elastic structure in fault slip estimates

Théa Ragon ⬤ and Mark Simons

Seismological Laboratory, California Institute of Technology, 1200 *E. California Blvd., Pasadena, CA 91125, USA. E-mail:* tragon@caltech.edu

SUMMARY

Earthquake source estimates are affected by many types of uncertainties, deriving from observational errors, modelling choices and our simplified description of the Earth's interior. While observational errors are often accounted for, epistemic uncertainties, which stem from our imperfect description of the forward model, are usually neglected. In particular, 3-D variations in crustal properties are rarely considered. 3-D crustal heterogeneity is known to largely affect estimates of the seismic source, using either geodetic or seismic data. Here, we use a perturbation approach to investigate, and account for, the impact of epistemic uncertainties related to 3-D variations of the mechanical properties of the crust. We validate our approach using a Bayesian sampling procedure applied to synthetic geodetic data generated from 2-D and 3-D finite-fault models. We show that accounting for uncertainties in crustal structure systematically increases the reliability of source estimates.

Key words: Inverse theory; Probability distributions; Earthquake source observations.

1 INTRODUCTION

We rely on inferences of subsurface fault slip to provide important insights after major earthquakes. More generally, we often use these images to explore the physics of the seismic source as well as post-seismic phenomena. We thus need these inferred images to be as accurate as possible, but we also need to be able to describe their limits.

Source estimates are constrained by the quality and quantity of observations, but are also severely impacted by the way we build the forward model and by any other prior information we include in the problem. Many authors have demonstrated that any change in the characteristics of the forward model (which include source parametrization but also description of the Earth's interior) may lead to variations in the inferred source properties (e.g. Beresnev 2003; Hartzell *et al.* 2007; Yagi & Fukahata 2008; Hsu *et al.* 2011; Duputel *et al.* 2014; Razafindrakoto & Mai 2014; Gallovič *et al.* 2015; Diao *et al.* 2016; Mai *et al.* 2016). Yet, our understanding of Earth's interior structure will always remain uncertain, and thus will always be susceptible to include biases in inferred source properties.

One obvious way to limit the biases deriving from our imperfect description of the Earth is to make the description as close as possible to the reality. Many authors thus describe the crustal structure as horizontally layered to evaluate the deformation induced at the surface using simple and efficient methods (e.g. Sato 1971; Sato & Matsu'ura 1973; Jovanovich *et al.* 1974; Virieux 1986; Pan 1999; Zhu & Rivera 2002). Yet, the uncertainties in elastic properties within each layer have been shown to significantly impact source models (e.g. Savage 1987; Cattin *et al.* 1999; Wald & Graves 2001; Simons *et al.* 2002; Masterlark 2003; Hearn & Bürgmann 2005;

Schmalzle *et al.* 2006; Hartzell *et al.* 2007; Duputel *et al.* 2014; Razafindrakoto & Mai 2014).

Crustal structure is usually more complex than just horizontally layered. In subduction zones, for example, interfaces are probably not horizontal. Seismic faults can border sedimentary basins and act as interfaces between regions with vastly different elastic properties. Similarly, significant velocity contrasts can be observed across and along major strike-slip faults such as the North Anatolian Fault (Turkey) or the San Andreas Fault (CA, USA, e.g. McGuire & Ben-Zion 2005; Ozakin *et al.* 2012; Najdahmadi *et al.* 2016; Share & Ben-Zion 2016; Zeng *et al.* 2016; Qiu *et al.* 2017; Share & Ben-Zion 2018; Agostinetti *et al.* 2020). Faults can also be surrounded by a highly fractured and thus more compliant medium than the regional host rock (e.g. Ben-Zion & Sammis 2003; Faulkner *et al.* 2003; Mitchell & Faulkner 2009; Sagy & Brodsky 2009; Faulkner *et al.* 2010). Seismic and boreholes observations suggest that the crust is inhomogeneous at all scales (e.g. Wu & Aki 1985; Levander & Holliger 1992; Dolan *et al.* 1998; Marsan & Bean 2003). Material property heterogeneities exist at all scales in three dimensions and this complexity in turn affects our estimates of the source (e.g. Wald & Graves 2001; Simons *et al.* 2002; Liu & Archuleta 2004; Zhao *et al.* 2004; Hartzell *et al.* 2010; Trasatti *et al.* 2011; Hsu *et al.* 2011; Gallovič *et al.* 2015; Williams & Wallace 2018). Fault geometry and its parametrization, as well as the inclusion of topographic effects, can also significantly impact inferred source properties (e.g. King & Nabelek 1985; Zhang *et al.* 1991; Bouchon *et al.* 1998; Aochi & Madariaga 2003; Masterlark 2003; Lee *et al.* 2006; Moreno *et al.* 2009; Hsu *et al.* 2011; Wei *et al.* 2011; Candela *et al.* 2012; Perrin *et al.* 2016a; Pizzi *et al.* 2017; Zielke *et al.* 2017; Williams & Wallace 2018; Langer *et al.* 2019, 2020).

Numerous numerical approaches to simulating the deformation caused by a seismic source embedded within a complex Earth structure model are now available, and are becoming increasingly computationally efficient (e.g. Komatitsch & Tromp 2002; Tromp *et al.* 2005; Parker *et al.* 2008; Aagaard *et al.* 2013; Gharti *et al.* 2019). Nevertheless, these methods remain more computationally demanding than simply assuming layered elastic structures and planar faults. Furthermore, even complicated 3-D models will be simplifications, or fuzzy reflections, of the true Earth's interior.

Another way to limit the biases deriving from our model approximations is to explicitly account for their imperfections. Methods have been proposed to account for the uncertainty of the Green's functions deriving from our poor knowledge of the Earth's interior. Yagi & Fukahata (2011), Duputel *et al.* (2012), Razafindrakoto & Mai (2014) and Hallo & Gallovič (2016, 2020) account for uncertainties in crustal structure, source time functions or centroid location, for waveform finite fault inversions. Jiang & Simons (2016) account for uncertainties in tsunami propagation. Duputel *et al.* (2014) proposed to derive uncertainties in the Green's functions from small perturbations of the crustal structure. We previously built on this approach in Ragon *et al.* (2018, 2019) to account for uncertainties in the fault geometry. These solutions have only been applied to layered heterogeneities. Accounting for uncertainty in horizontally layered medium will not be sufficient in many cases, such as a subduction zone, a vertical interface, or even a fault surrounded by a damage zone. In this study, we use the approach proposed by Duputel *et al.* (2014) to investigate the uncertainty in 3-D heterogeneities.

We demonstrate that small perturbation theory can be applied to account for 3-D heterogeneities of the crustal structure. To do so, we start by analysing simple 2.5-D toy models that allow us to investigate combinations of vertical and horizontal interfaces while avoiding any 3-D complexity in the interpretation of our results. In particular, we explore the cases where an infinite strike-slip fault is bounding two regions of different elastic properties, with or without layering and with or without a compliant fault zone. Then, we validate our results with a realistic finite-fault toy model embedded in a half-space perturbed by vertical interfaces. We show that accounting for epistemic uncertainties largely mitigates the impact of simple crustal 3-D heterogeneity in source estimates. Our results suggest that the presented approach will be efficient and easily implemented for uncertainty acknowledgement in complex 3-D crustal structures, such as velocity models derived from tomographic observations.

2 TOOLS AND METHODS

2.1 Uncertainties in model predictions due to inaccuracies of the forward model

When solving for a source model $\mathbf{m}$, our estimates will primarily depend on the observations $\mathbf{d}_{obs}$ and on the *a priori* calculated Green's functions, $\mathbf{G}$. Additionally, estimated model parameters will be influenced by both observational and epistemic errors, and by any other prior assumption. Epistemic errors stem from our imperfect knowledge, or simplification, of the parameters describing the forward problem, such as crustal properties (e.g. rheology), fault geometry or regional characteristics (e.g. topography).

If we assume that the real surface displacement $\mathbf{d}$ follows a Gaussian distribution centred on the predictions $\mathbf{d}_{pred} = \mathbf{G}(\mathbf{m})$ within an uncertainty described by a covariance matrix $\mathbf{C}_\chi$, we can determine the discrepancies between observations and predictions of the

model $\mathbf{m}$ by a misfit function (Tarantola 2005; Minson *et al.* 2013, 2014; Duputel *et al.* 2014) of the form

$$\chi(\mathbf{m}) = \frac{1}{2}[\mathbf{d}_{obs} - \mathbf{G}(\mathbf{m})]^T \cdot \mathbf{C}_\chi^{-1} \cdot [\mathbf{d}_{obs} - \mathbf{G}(\mathbf{m})], \tag{1}$$

Often, $\mathbf{C}_\chi$ is assumed to only describe the observational covariances $\mathbf{C}_d$.

However, accounting for epistemic errors is often necessary to infer reliable and robust source estimates (Minson *et al.* 2014; Duputel *et al.* 2014; Ragon *et al.* 2018, 2019). In this case, the misfit covariance becomes

$$\mathbf{C}_\chi(\mathbf{m}) = \mathbf{C}_d + \mathbf{C}_p(\mathbf{m}), \tag{2}$$

where $\mathbf{C}_p(\mathbf{m})$ is a covariance matrix describing the uncertainty of the predictions, and thus which depends on the resulting source model. The calculation methodology for $\mathbf{C}_p(\mathbf{m})$ is detailed in Duputel *et al.* (2014) and Ragon *et al.* (2018); in the following paragraphs, we only summarize the essential steps.

We assume an uncertain and presumably inaccurate set of parameters Ψ_{prior} describing generic properties of the forward model Ψ. We can explore the prediction uncertainty by assuming that the predictions $\mathbf{d}_{pred} = \mathbf{G}(\Psi, \mathbf{m})$ for the generic properties Ψ can be approximated by linearized and small perturbations of the predictions $\mathbf{G}(\Psi_{prior}, \mathbf{m})$ for the fixed set of parameters Ψ_{prior} and the unknown source parameters $\mathbf{m}$:

$$\mathbf{G}(\Psi, \mathbf{m}) \approx \mathbf{G}(\Psi_{prior}, \mathbf{m}) + \mathbf{K}_\Psi(\Psi_{prior}, \mathbf{m}) \cdot (\Psi - \Psi_{prior}), \tag{3}$$

where the matrix $\mathbf{K}_\Psi(\Psi_{prior}, \mathbf{m})$ is the sensitivity kernel of the predictions with respect to the set of parameters.

If we want to incorporate $\mathbf{C}_p$ into the source estimation problem, the calculation requires the prior choice of a source model $\mathbf{m}_{prior}$. We choose to update $\mathbf{m}_{prior}$ at every step of the sampling process. In our case, Ψ_{prior} is a set of shear moduli values, which are so-called Jeffreys parameters (i.e. Tarantola 2005), we thus assume the prior distribution of Ψ to be log-normal. The prediction matrix can then be written as (Duputel *et al.* 2014)

$$\mathbf{C}_p = \mathbf{K}_\Psi \cdot \mathbf{C}_\Psi \cdot \mathbf{K}_\Psi^T, \tag{4}$$

where

$$\mathbf{K}_\Psi = \mathbf{K}_\Psi^G \cdot \mathbf{m}_{prior}, \tag{5}$$

$$(\mathbf{K}_\Psi^G)_{ijk}(\Psi_{prior}) = \frac{\partial G_{ik}}{\partial \ln \Psi_j}(\Psi_{prior}), \tag{6}$$

and $\mathbf{C}_\Psi$ is the standard deviation of the log-normal prior distribution of parameters Ψ. We can pre-compute the sensitivity kernels $\mathbf{K}_\Psi^G$ without any dependence on the assumed model $\mathbf{m}_{prior}$. Finally, note that, unlike the data covariance matrix $\mathbf{C}_d$, the prediction covariance matrix $\mathbf{C}_p$ usually has significant off-diagonal terms.

2.2 Description of the forward model

We want to investigate the impact of 3-D uncertainties in crustal properties, and in particular lateral elastic heterogeneities, on inferred slip models. We start by analysing a 2.5-D toy model, which consists of an infinitely long vertical strike slip fault embedded in an elastic half-space (Fig. 1). The half-space can either be homogeneous, or contain vertical and/or lateral heterogeneities.

The assumed fault extends infinitely along strike, and slips uniformly with an amplitude of 10 m from the free surface to a depth of 10 km. The fault is discretized into 20 elements. The surface
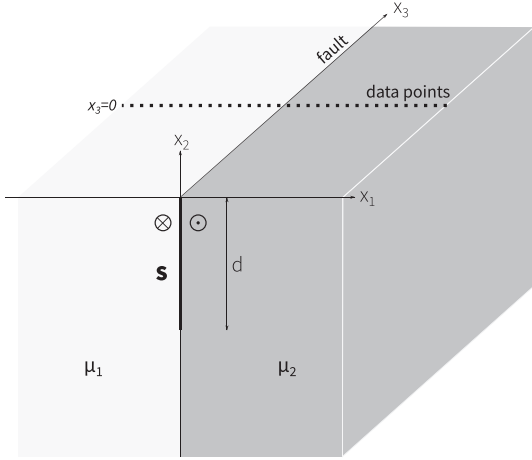
Figure 1. Description of the toy model used in the study. We assume an infinitely long vertical strike-slip fault, with uniform 10 m slip, **s**, from the free surface to a depth d of 10 km. The surface displacement is calculated at 100 distinct locations distributed linearly and perpendicularly to the fault strike, up to 40 km away from the fault in both directions. Here, the fault is also a lateral interface between two crustal domains of different elastic properties.

displacement is calculated at 100 distinct locations distributed perpendicular to the fault strike, up to 40 km away from the fault in both directions (Fig. 1).

We choose to study an infinitely long and vertical strike slip fault because analytical solutions for the surface displacement induced by the equivalent dislocation problem have been proposed for various elastic structures (e.g. Rybicki 1971; Segall 2010), which is computationally efficient for the simple tests we performed. When the equivalent dislocation problem does not allow us to easily calculate analytical solutions, we compute surface displacements with the finite-element code Pylith (Aagaard *et al.* 2013), as detailed bellow. We also perform some additional tests assuming a dip-slip vertical fault for simplicity, validating our conclusions for plane strain conditions.

2.2.1 Analytical solutions for slip on an infinite strike-slip fault

For dislocations in simple elastic structures, such as a homogeneous half-space or with a single vertical or horizontal interface, the expressions of the surface displacement and sensitivity kernels are directly derived from the solutions proposed by Rybicki & Kasahara (1977) and Segall (2010), and are detailed in Appendix A.

When we investigate an elastic structure with several heterogeneities, we approximate the analytical solution with a moduli perturbation approach (e.g. Du *et al.* 1994; Cervelli *et al.* 1999; Segall 2010). This approach allows us to approximate the solution for a multi-interfaces elastic structure as a superposition of solutions calculated for single-interface structures (e.g. Mahrer 1981), approximations that only hold if the variations in shear moduli are small (see Appendix A4, and next paragraph for validation examples).

2.2.2 Finite-element modelling for slip on an infinite strike-slip fault

For more complex elastic structures, and to validate our analytical approximations, we use the finite-element code Pylith (Aagaard

et al. 2013) with the grid specifications detailed in Fig. S1 and in Table S1. We approximate the infinitely long fault with a 2000-km-long fault (the fault is 200 times longer than wide). As a validation example for our approximate analytical solutions, we use an elastic structure composed of two horizontal interfaces and one vertical interface, as described in Appendix A4 and Fig. A1. In this case, the shear moduli ratios are realistic for typical values found in the crust ([0.3,0.9]), ensuring the variations in shear moduli remain relatively small. The approximate analytical solution and the FEM-based solution agree at a level of a few percent (Figs S2 and S3). The similarity between the solutions justifies the use of the approximations in the following tests.

2.3 Bayesian sampling of the inverse problem

In this study, we explore the full solution space of the slip models in order to draw samples from the most plausible models. The sampling is performed with a Bayesian approach implemented in the AlTar package, a reformulation of the code CATMIP (Minson *et al.* 2013). AlTar combines the Metropolis algorithm with a tempering process to iteratively sample the solution space. A large number of samples are tested in parallel at each transitional step, followed by a resampling step that allows efficient exploration of complex solution spaces.

The ability of each model parameter to solve the source problem is evaluated through repeated updates of the probability density functions (PDFs)

$$f(\mathbf{m}, \beta_i) \propto p(\mathbf{m}) \cdot \exp[-\beta_i \cdot \chi(\mathbf{m})], \qquad (7)$$

with **m** a representative sample, $p(\mathbf{m})$ the prior information on this sample, $\chi(\mathbf{m})$ being the misfit function, i corresponding to each iteration and β evolving dynamically from 0 to 1 to improve the efficiency of the parameter space exploration (Minson *et al.* 2013).

The final output from our Bayesian sampling procedure is an ensemble of models sampling the posteriors PDF. To explore the results, we consider derived probabilistic variables, such as the mean of the sampled models and the associated posterior uncertainty.

We do not impose any spatial regularization or smoothing to narrow down the sampling space. Additionally, the use of probabilistic values (such as the mean) can be seen as performing a posterior smoothing of the solution space. As prior information, we impose a uniform distribution $p(\mathbf{m}) = \mathcal{U}(0 \text{ m}, 25 \text{ m})$ for the strike-slip parameters, and a restrictive Gaussian prior distribution centred on zero for the dip-slip parameters, $p(\mathbf{m}) = \mathcal{N}(-1 \text{ m}, 1 \text{ m})$.

3 AN INFINITE STRIKE SLIP FAULT EMBEDDED IN A 2-D-VARYING MEDIUM

All of our tests follow the same procedure. We compute synthetic surface displacements at specified locations using the assumed true elastic structure. In most of the following results, no noise is added to the synthetic observations, but we also perform some tests with various noise realizations in Section 3.3. We assume a diagonal data covariance matrix $\mathbf{C}_d$ characterized by a variance of 1 m^2 when no noise is added to the synthetic data, or by the noise variance otherwise. We perform a first inversion of the synthetic data assuming the true Green's functions (GFs) to validate our inversion process. Then, we use an incorrect elastic structure (homogeneous or a simplification of the true structure) to calculate inaccurate GFs, and
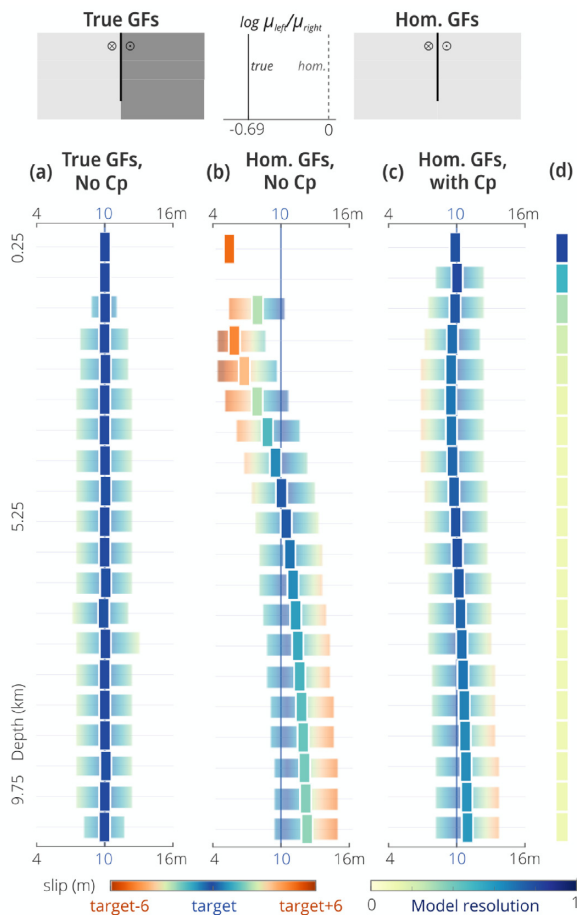
Figure 2. Inferred slip amplitude characterized by its mean (vertical rectangle) and standard deviation (σ), for an infinite strike slip fault bounding two media of shear moduli μ_1 and μ_2. In (a), the slip is inferred assuming the true elastic structure with $\mu_1/\mu_2 = 0.5$. In (b) and (c), the crustal structure is assumed to be homogeneous, but in (c) epistemic uncertainties are accounted for. The target slip is a uniform slip distribution of 10 m in amplitude (blue vertical line). (d) Model resolution (e.g. Menke 2012) for each parameter. At the top of the figure, schematic views of the true and assumed crustal structures are presented and colour-coded, the more compliant the medium, the lighter the grey.

solve for the slip distribution assuming these inaccurate GFs. Finally, we repeat the inversion using inaccurate GFs, but accounting for epistemic uncertainties.

For every test, we represent the results of the three sampling procedures (for instance, refer to Fig. 2). We define every inferred parameter with its mean and a range of plausible values (within 1σ of the mean value), which are colour-coded corresponding to their distance to the target model (10 m).

3.1 Fault bounding two media

Although elastic properties across a fault are usually relatively similar (e.g. Ben-Zion & Andrews 1998), some portions of strike slip faults may separate crustal domains of different properties. For instance, Jolivet *et al.* (2009) modelled the interseismic velocity of a section of the San Andreas fault using an asymmetric half-space with a shear moduli ratio (μ_1/μ_2) of ~0.66. A similar ratio has been found by Reinoza *et al.* (2015) for the El Pilar fault in Venezuela. Pichon *et al.* (2005) found very large rigidity ratios across some

portions of the North Anatolian and Great Sumatra faults, that may be caused by elasticity contrasts with ratios as small as 0.1 (but other parameters may be at play too). Bulut *et al.* (2012); Ozakin *et al.* (2012); Najdahmadi *et al.* (2016) also found velocity contrasts across the North Anatolian fault, although lower than the aforementioned values. In this first case, we consider an elasticity contrast across the fault with a ratio of 0.5.

3.1.1 Results

As expected, when assuming true GFs, the target model is well estimated (Fig. 2a), although with a relatively large posterior uncertainty (up to $1\sigma = 3$ m), associated with the low model resolution at increasing depths (Fig. 2d). When assuming a homogeneous elastic structure and neglecting epistemic uncertainties, the target model is poorly recovered. The inferred slip is particularly off in the shallow part of the fault, probably because the surface displacements, calculated with different structures, diverge the most within a few kilometres of the fault (Fig. S4). In contrast, accounting for epistemic uncertainties allows us to correctly estimate the target model. Typically, sampling procedures which account for $\mathbf{C}_p$ (for any type of 2-D epistemic uncertainty, Ragon *et al.* 2018, 2019) prevent the predictions from being overconfident in the data. Our test follows the same scheme: including $\mathbf{C}_p$ yields larger residuals between predictions and synthetic observations (Fig. S4), although the inferred model is relatively unbiased.

3.1.2 Non-uniform target slip distribution

Although our toy models are far from replicating the behavior of a real fault, we present here a more realistic subsurface slip distribution, which shows some shallow slip deficit and tapers at depths to become null below 8-km-depth (Fig. 3). Additionally, spatially correlated noise is added to the analytically calculated synthetic data (Fig. S6). If assuming a correct crustal structure, while the target slip deficit is well inferred down to 8-km-depth, the downdip limit of the slip is poorly recovered, probably because of the poor model resolution (fig. 2, also refer to the tests performed in Duputel *et al.* 2014). As expected, if the crustal structure is approximated and uncertainties neglected, inferred slip is off at all depths. Often, the target is not even within uncertainty range from the mean slip. Introducing $\mathbf{C}_p$ yields accurate results, slip values being very close to the ones inferred with the true structure.

In the case where there is a vertical interface in crustal properties, accounting for epistemic uncertainties allows us to properly infer the target slip, even if non-uniform. Of course, the accuracy of the results will depend on the sensitivity of the data. For simplicity, we only present the non-uniform target slip case with the vertically heterogeneous example. The conclusions that follow will be similar for uniform or non-uniform slip distributions, as Duputel *et al.* (2014) demonstrated that a layered crustal structure also impacts the recovery of a non-uniform slip.

3.2 Lateral and vertical heterogeneity

In this example, the crustal structure is now composed of two compliant layers above a half-space, the compliance decreasing with depth. Additionally, the fault structure still acts as a vertical interface. The elasticity contrast (given as a ratio) across the fault varies from 0.6 (shallow layer) to 0.8 (at depth). Similarly, the elasticity
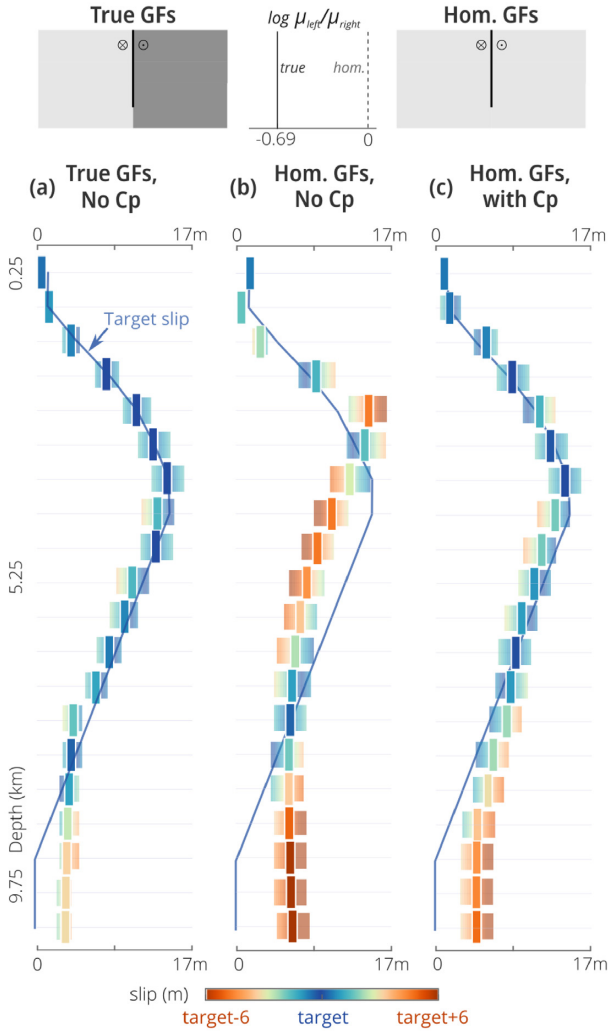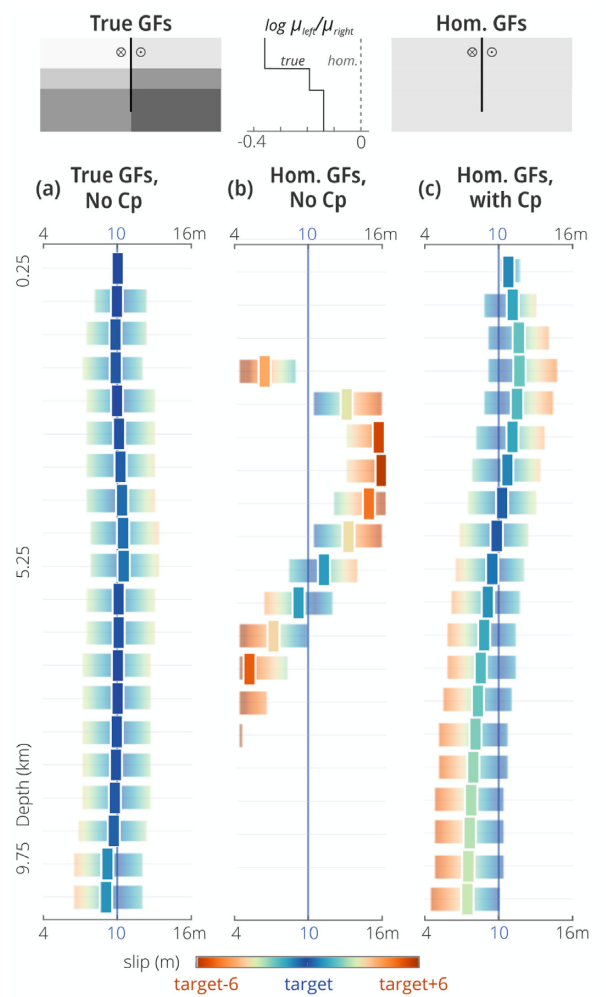
Figure 3. Same as Fig. 2 but with a depth-varying target slip distribution. The target slip is shown with a blue line. Note that the x-axis scale has a larger extent than in the other figures.

Figure 4. Comparison of inferred models neglecting or including $\mathbf{C}_p$. Inferred slip amplitude characterized by its mean (in between vertical white bars) and standard deviation (σ), for an infinite strike slip fault embedded in a heterogeneous media, composed of 2 layers over a half-space and a vertical heterogeneity (Fig. A1). In (a), the slip is inferred assuming the true values for the shear moduli of each domain. In (b) and (c), the crustal structure is assumed to be homogeneous, but in (c) epistemic uncertainties are accounted for. The target slip is a uniform slip distribution of 10 m in amplitude. At the top of the figure, schematic views of the true and assumed crustal structures are presented and colour-coded, the more compliant the medium, the lighter the grey.

contrast across horizontal interfaces varies from 0.6 (shallow layer) to 0.8 (at depth).

Green's functions and uncertainties have been calculated with the analytical approximation only. The uncertainty is thus calculated for every layer and for every vertical domain independently, which are then combined.

3.2.1 Results

When assuming a homogeneous crustal structure in estimating slip (Fig. 4), the increased complexity of the true crustal structure makes the estimates very poor (Fig. 4b) Interestingly, the range of plausible models does not in fact include the target model (the mean parameters are not within 1σ of the target parameters). As expected, accounting for uncertainties reliably improves the inferred models. Mean estimates are still slightly off for some parameters, especially at depth, but the target model remains amongst the plausible models. When $\mathbf{C}_p$ is not accounted for, deep oscillations of the inferred slip amplitudes are required for the predictions to approach the observations (Fig. S7). In contrast, the predictions of the case with $\mathbf{C}_p$ stay very close to what they would be in a homogeneous case.

What happens if we assume a layered crust instead of a homogeneous one? In this next case (Fig. 5), the fault is no longer an interface and the crust replicates one side of the true structure. The assumed structure being closer to the true one, the estimated model is closer to the target model than in the previous tests. However, the target model remains out of the plausible set of models, especially at depth (Fig. 7b). In contrast, accounting for uncertainties yields a well recovered target model. Note that the model estimated without $\mathbf{C}_p$ is worst than the model estimated in the vertical interface case (Fig. 2b), although the two cases can be thought as equivalent (only the vertical interface missing from the assumed crust). This difference is due to the fact that, in the layered case, the elasticity ratio across the fault varies with depth, contrary to when there is a vertical interface only.
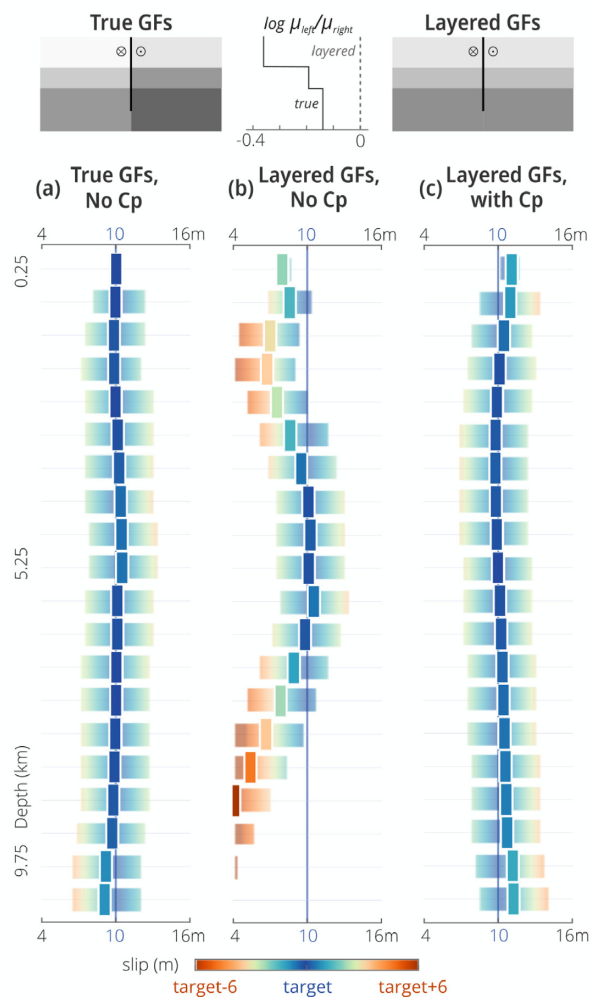
Figure 5. Same as Fig. 4, with, in (b) and (c), the crustal structure assumed to be layered, and, in (c), epistemic uncertainties calculated analytically. The assumed layered crustal structure replicates the left side of the true structure.

This series of examples suggest that we should always use a layered crustal structure, even in the static case, instead of homogeneous structures, as already demonstrated by numerous authors (e.g. Trasatti *et al.* 2011; Hearn & Bürgmann 2005; He *et al.* 2003; Wald & Graves 2001, and other references in section 1). Of course, accounting for uncertainties, either using homogeneous or layered crust, will yield more robust results.

3.3 Different velocity gradient on either side of the fault

In the previous examples, the vertical gradient of the seismic velocity has been assumed to be similar on either side of the fault. In reality, however, the gradient can vary. For instance, the slope of compliancy gradient can be different across the fault, or the gradient can even be of different sign, as suggested by some observations of the San Andreas Fault near Parkfield (e.g. Agostinetti *et al.* 2020), across the San Andreas and San Jacinto Fault zones (e.g. Allam & Ben-Zion 2012) or the North Anatolian Fault (e.g. Yolsal-Çevikbilen *et al.* 2012; Kahraman *et al.* 2015).

In this toy model, we consider a crustal structure consisting of two layers above a half-space, the fault being a vertical interface. One side of the fault is characterized by a decreasing compliancy with depth (as in the previous layered case presented in Section 3.2),
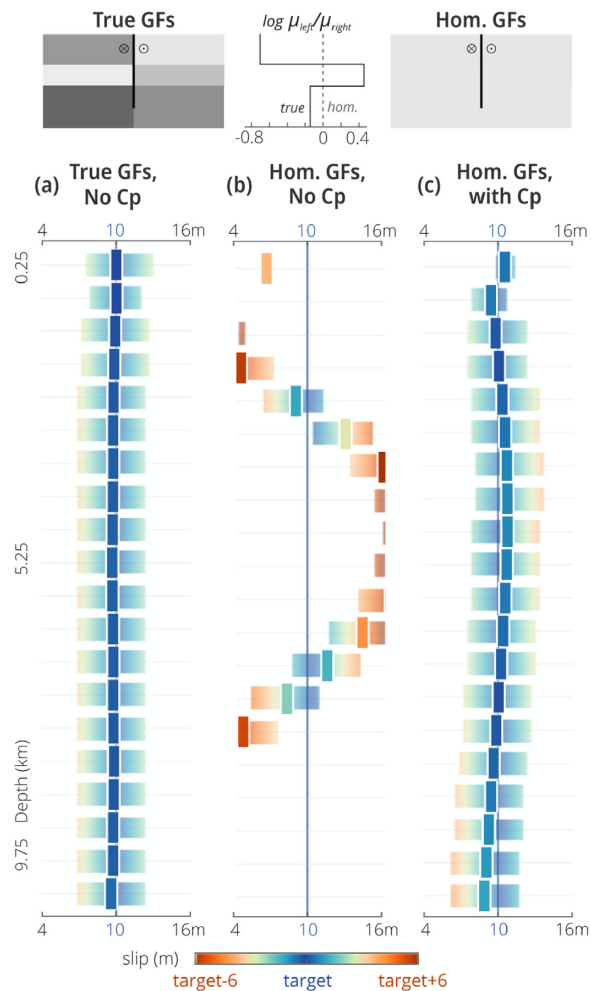
Figure 6. Comparison of inferred models neglecting or including C_p. Inferred slip amplitude characterized by its mean (in between vertical white bars) and standard deviation (σ), for an infinite strike slip fault embedded in a heterogeneous media, composed of 2 layers over a half-space and a vertical heterogeneity, the velocity gradients being different in either side of the fault. In (a), the slip is inferred assuming the true values for the shear moduli of each domain. In (b) and (c), the crustal structure is assumed to be homogeneous, but in (c) epistemic uncertainties are calculated for each domain independently and accounted for. The target slip is a uniform slip distribution of 10 m in amplitude. At the top of the figure, schematic views of the true and assumed crustal structures are presented and colour-coded, the more compliant the medium, the lighter the grey.

whereas the other side is characterized by a sign change in the velocity gradient (see in Fig. 6). The elasticity contrast across the fault varies from 0.6 (shallow layer) to 0.8 (at depth). The elasticity contrast across horizontal interfaces varies from 0.5 (shallow parts and sign change side) to 0.8 (at depth).

The Green's functions are derived from the FEM (refer to Section 2.2.2). Uncertainties can be calculated by perturbing each of the six subdomains independently using the FEM. Another option would be to estimate the uncertainties as in the layered case (Section 3.2), that is by perturbing layer by layer, and combine these uncertainties to the ones derived for the two vertical domains on each side of the fault.
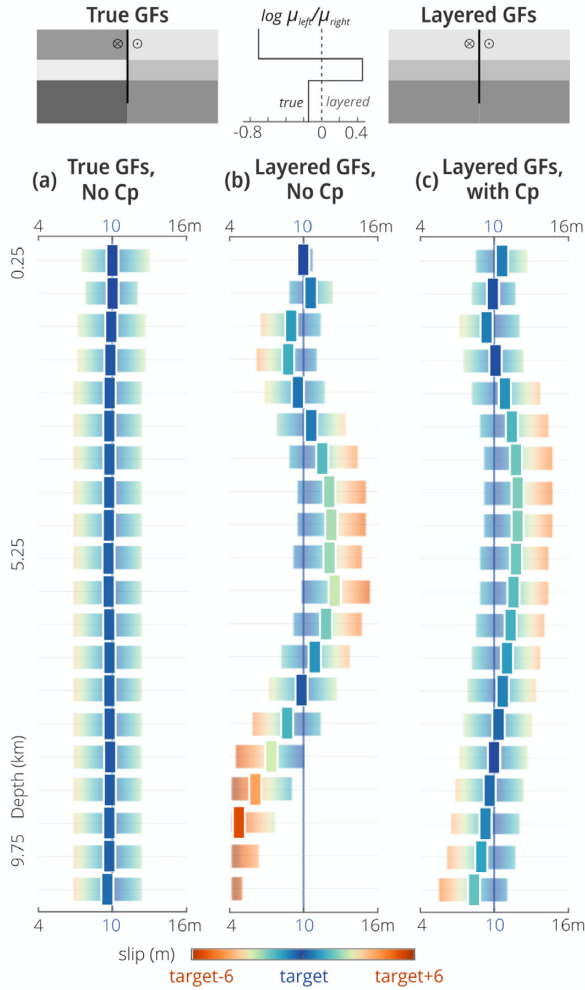
Figure 7. Same as Fig. 6, with, in (b) and (c), the crustal structure assumed to be layered, and, in (c), epistemic uncertainties calculated by layers and vertical domains. The assumed layered crustal structure replicates the right side of the true structure.

3.3.1 Results

For the first slip inference, we assume the crustal structure to be homogeneous (Fig. 6). Of course, when $\mathbf{C}_p$ is ignored, the inferred slip model is very far from the target model, the set of plausible parameters even excluding the target values. In contrast, when introducing uncertainties in the inference process, calculated independently for each domain, the target model is well retrieved (Fig. 6c). Interestingly, the estimated slip model is closer to the target model than in the layered case (Fig. 4c), and yet in the latter case the true crustal structure was less complex. This suggests that calculating uncertainty for each domain is more efficient at reflecting the sensitivity of the Green's functions than using the uncertainty of layers. Even more clearly than for the previous examples, without $\mathbf{C}_p$ the predictions fit the observations very well (Fig. S8) despite a woefully incorrect slip model. The fit is worse when uncertainties are accounted for, whereas the inferred model is closer to the target.

For the next toy model, we calculate the crustal uncertainty as in Section 3.2, that is for each layer and for the two vertical domains on each side of the fault, still deriving it from the FEM simulations. We also assume a layered crust, using the elasticity values of the decreasing compliance side of the true structure (Fig. 7). Without $\mathbf{C}_p$, the estimated slip is not too far from the target model, with the

exception of the deepest subfaults, probably because the assumed crustal structure is closer to the true one. With $\mathbf{C}_p$ included, the target model is well recovered. Interestingly, the result is slightly farther from the target than in the former test, where epistemic uncertainties were calculated independently for each crustal domain. Indeed, deriving epistemic uncertainties as in the layered case does not allow us to account for variations in velocity gradients across the fault and within one layer.

If we assume a layered structure with elasticity taken as the average of the true structure (layer by layer, Fig. S9), and assuming the same uncertainty as in Fig. 7, both results with and without $\mathbf{C}_p$ are even closer to the target model. Of course, it would be almost impossible to know the average structure in a real case.

We also perform some tests adding various realizations of noise to the synthetic surface displacement. When noise is added, we increase observational uncertainties accordingly. For the first case, noise consists of Gaussian noise combined with spatially correlated noise with a standard deviation being of 6 per cent of the maximum surface displacement. Assuming a homogeneous crustal structure, results are similar whether or not noise is added, although inferred models are slightly less accurate even with correct Green's functions. Introducing epistemic uncertainties (calculated for independent domains) yields slightly less robust slip estimates at shallowest depths (Figs S10 and S11), probably because of the noise affecting near fault observations. For the second case, we use a different realization of noise whose standard deviation is of 9 per cent of the maximum surface displacement. Again, the results are very similar to the noise-free case, assuming a homogeneous crust (Figs S12 and S13). Unsurprisingly, results are similar to the noise-free ones if assuming a layered crust (again using the second noise realization and epistemic uncertainties calculated from independent domains, Fig. S14). These tests confirm that our results are robust whether noisy observations are considered or not.

Finally, we also investigate if our conclusions hold for a dip-slip fault. We assume a vertical fault for simplicity, and a target model which consists in a 10 m amplitude reverse slip. Synthetic surface displacement and Green's functions are FEM-derived, and uncertainties are calculated by perturbing each of the six subdomains independently using the FEM. Assuming a layered crustal structure, our results replicate the ones of the strike-slip case: neglecting $\mathbf{C}_p$ leads to very poor estimates (Fig. S15b), with the target slip outside of the range of inferred plausible solutions (Fig. S16). In contrast, introduction of epistemic uncertainties results in a greatly improved inference (Fig. S15c).

3.4 Damage zone

Instead of an interface, observations of exhumed faults suggest that faults may be a volume composed of a core, where most of the deformation occurs, surrounded by a damage zone in which the deformation is smaller (e.g. Ben-Zion & Sammis 2003; Mitchell & Faulkner 2009; Sagy & Brodsky 2009; Faulkner *et al.* 2010). The damage zone is typically characterized by reduced elastic moduli relatively to surrounding rocks. The width of the inner and most damaged part of the fault zone is usually thought to reach a few hundreds of metres at its maximum (e.g. Mitchell & Faulkner 2009; Faulkner *et al.* 2010; Savage & Brodsky 2011; Mitchell & Faulkner 2012) although it can reach a kilometre in rare cases (e.g. Wilson *et al.* 2003; Gudmundsson 2007), but some observations might suggest that the outer and less damaged part could reach a few kilometres width (e.g. Faulkner *et al.* 2003; Wilson *et al.* 2003; Gudmundsson 2007;

Materna & Bürgmann 2016; Perrin *et al.* 2016b). Damage zones can have a non-negligible impact on rupture dynamics, stresses and slip estimates (e.g. Spudich & Olsen 2001; Faulkner *et al.* 2006; Barbot *et al.* 2008; Sammis *et al.* 2009; Huang & Ampuero 2011; Gabriel *et al.* 2013; Cappa *et al.* 2014; Huang *et al.* 2014; Perrin *et al.* 2016b; Gombert *et al.* 2017).

In this last toy model, we consider a, possibly unrealistic, setting in which the fault is embedded in a 2–4-km-wide damage zone of reduced elastic modulus. The damage zone reaches infinite depth and is characterized by an elastic ratio of 0.5 with the background shear modulus. The Green's functions and uncertainties are derived from the analytical solutions (after Segall 2010) presented in Appendix A5. We only investigate the sensitivity of the Green's functions to variations of the elastic properties of the damage zone, that is we only estimate prediction errors from the domain corresponding to the damage zone.

In the previous examples, the data points were distributed every 800 m. In this example, we increase the sampling of the data points around the fault to improve the sensitivity to the damage zone. Data points are thus distributed every 200 m within 5 km of the fault, still considering a total of 100 data points within 40 km of the fault. 14 or 28 data points are located within the damage zone for a 2 or 4 km wide zone, respectively.

3.4.1 Results

If the damage zone is 2 km wide, its effect on static slip estimates is very slight (Fig. S17), and   assuming a homogeneous crustal structure allows us to image correctly the target model. Still, accounting for uncertainties improves the results, even if it is not really necessary.

If we increase the width of the damage zone to 4 km, the number of data points sensitive to the properties of the damage zone are doubled. When assuming a homogeneous crustal structure, the estimated slip model is off (Fig. 8b). At the surface, the target model is not even amongst the range of plausible models. In contrast, accounting for uncertainties allows us to correctly infer the target slip. Note that we only account for the uncertainties related to the damage zone, which is reflected in Fig. S18 (uncertainty of the observations is within 2 km of the fault).

From our results, we suggest that if more than 10 per cent of the observations are located within the compliant damage zone, accounting for the damages and related uncertainty becomes necessary to infer reliable slip models. Some observations suggest that the properties of damage zones, including their elasticity and width, but also their presence, vary along strike (e.g. Materna & Bürgmann 2016; Perrin *et al.* 2016b). If there is along strike variability, accounting for epistemic uncertainties related to damage zones would also be efficient, as introducing uncertainty still yields robust results if the assumed structure is the true one (e.g. Ragon *et al.* 2018, 2019).

4   3-D FINITE-FAULT TOY MODEL

In this section, we investigate if the proposed methodology is still efficient in a real 3-D case. To this end, we build a 3-D toy model which consists in a finite vertical strike slip fault embedded in a heterogeneous medium.
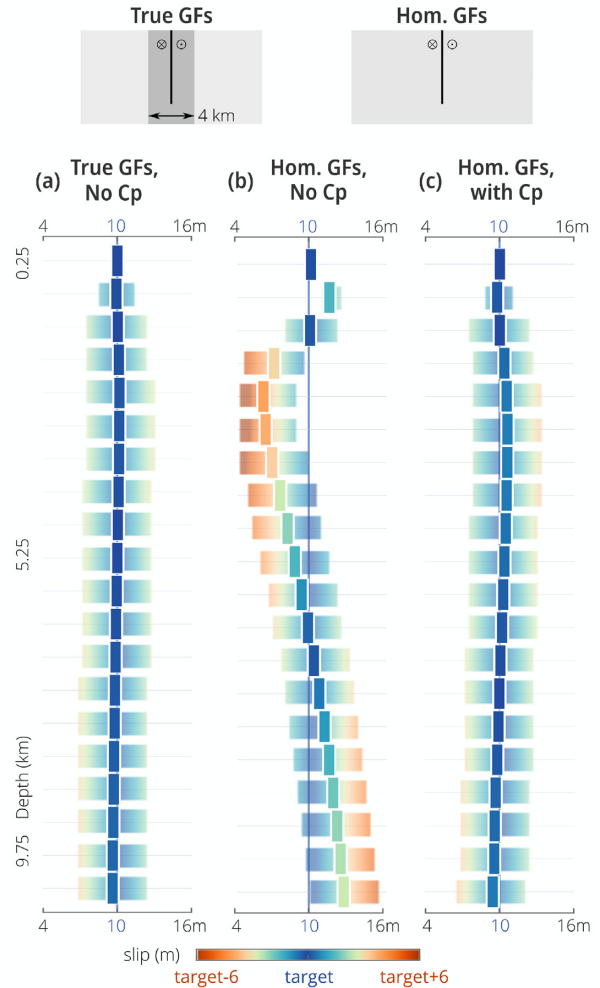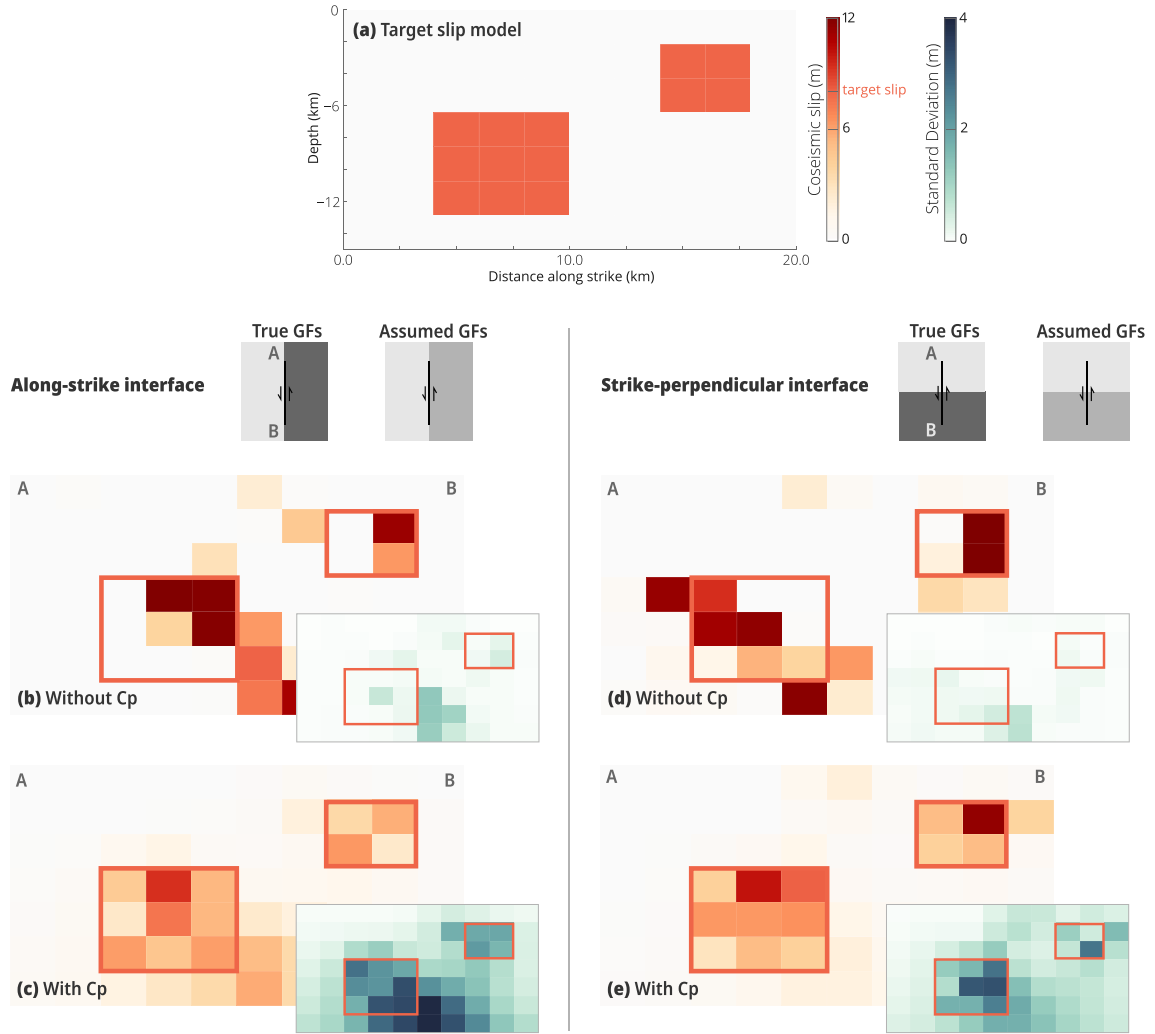

Figure 8. Comparison of inferred models neglecting and including C_p. Inferred slip amplitude characterized by its mean (in between vertical white bars) and standard deviation (σ), for an infinite strike slip fault embedded in a compliant fault zone in a homogeneous half-space. The width of the fault zone is 4 km. In (a), the slip is inferred assuming the true values for the shear moduli of each domain. In (b) and (c), the crustal structure is assumed to be homogeneous, but in (c) epistemic uncertainties are calculated for each domain independently and accounted for. The target slip is a uniform slip distribution of 10 m in amplitude. At the top of the figure, schematic views of the true and assumed crustal structures are presented and colour-coded, the more compliant the medium, the lighter the grey.

4.1 Setting of the finite-fault toy model

The strike slip fault is 20 km long and 15 km wide (i.e. downdip extent), and is embedded in a heterogeneous half-space. We consider that the half-space is divided into two regions by either a vertical along-strike interface, or a vertical strike-perpendicular interface. The vertical strike-perpendicular interface is unrealistic, but it is an extreme illustration of along strike variations of crustal properties that could be caused by a variety of factors, such as cross-cutting faults, inherited rheology, or the presence of fluids. The true shear moduli ratio between the two regions of the medium is 0.6. Each component of the surface displacement caused by the target strike-slip presented in Fig. 9(a) (equivalent to a M_w 6.7 event) is produced at 200 locations randomly distributed 20 km around the fault. Gaussian noise and spatially correlated noise (drawn from

Figure 9. Comparison of inferred strike-slip amplitudes neglecting and including $\mathbf{C}_p$ in the 3-D case. The target slip model is shown in (a). When the true crustal structure has an along-strike interface, inferred slip amplitude and posterior uncertainty are shown in (b) and (c), respectively neglecting and accounting for $\mathbf{C}_p$. When the true crustal structure has a strike-perpendicular interface, inferred slip amplitude and posterior uncertainty are shown in (d) and (e), respectively neglecting and accounting for $\mathbf{C}_p$. Schematic map views of the true and assumed crustal structures are presented and colour-coded, the more compliant the medium, the lighter the grey.

multivariate Gaussian distributions) have been added to the observations. We assume that the observational error is of 6 per cent of the displacement amplitude. Target predictions, Green's functions and uncertainties are derived from FEM simulations with the grid specifications detailed in Fig. S19 and   in Table S2, even when assuming a homogeneous crustal structure.

For our tests, we assume that the ratio of shear moduli between the two regions of the medium is 0.9 (and thus that the two regions are elastically more similar than what they are in reality). We use a uniform prior distribution $p(\mathbf{m}) = \mathcal{U}(0 \text{ m}, 25 \text{ m})$ for the strike-slip parameters, and a Gaussian prior distribution centred on zero for the dip-slip parameters $p(\mathbf{m}) = \mathcal{N}(\text{-2 m}, 2 \text{ m})$.

4.2 Results

First, we investigate the case when the true structure is homogeneous, and when the assumed structure mirrors the true one. In this perfect case, the inferred mean strike-slip amplitude is close to the target model, even if it does not exactly replicate it (Fig. S20). Although the noise is accounted for in $\mathbf{C}_d$, the discrepancy between

the mean and the target model is probably due to a combination of the observational noise and poor model resolution at depth. The random distribution of the data plays a significant role in the imperfection of the range of recovered models. Nonetheless, the target model lies within the inferred models.

4.2.1 Fault bounding two media

As expected, the inferred mean strike-slip amplitudes significantly differs from the target model when uncertainties are not accounted for (Fig. 9b). The posterior uncertainty (1σ, Fig. 9b) is low, and thus the target model does not lie within 1σ or even 2σ of the mean model. Similarly, the mean dip-slip amplitudes largely (up to 7 m) vary around the target value of 0 m (Fig. S21a). In contrast, accounting for $\mathbf{C}_p$ yields estimated amplitudes closer to the target model, the target being amongst the inferred samples (Figs 9c and S21c). The standard deviation associated with the estimated amplitudes is largely increased.

Some particularly large amplitudes are imaged in between the two slip patches, especially when neglecting $\mathbf{C}_p$. These large amplitudes, probably primarily driven from inaccurate GFs, possibly also derive from the lack of observations around the central part of the fault (Figs S22a and c). When $\mathbf{C}_p$ is neglected, predictions are overconfident in the observations (Figs S22a and c).

4.2.2 Strike-perpendicular vertical interface

Results are similar when the interface is perpendicular to the strike direction, inferred models not replicating the target when uncertainties are neglected, while the target is approached when uncertainties are accounted for (Figs 9d,e, S21b and d).

Unlike the previous example, the target slip patch on the A side of the fault (Fig. 9d) is not affected by any variation in the elastic structure. Alluding to the physical intuition that a non-null gradient of the shear modulus will have no impact on a displacement if they are not collocated, we could postulate that the slip on side A would be inferred correctly, whether the elastic structure on side B is correct or not. Yet, we show that $\mathbf{C}_p$ is required to correctly infer the target model on both sides. Obviously, the displacement produced at the surface by the slip patch A is affected by the variation of elastic properties in side B, in turn disturbing the estimates of slip amplitude. Another explanation lies in the correlation between model parameters: estimates of slip on side B are probably more affected by a variation of elastic properties of side B, and in turn can alter the slip estimates on side A.

Models inferred without epistemic uncertainties, for any type of interface (Figs 9b and d), are particularly rough. We choose not to include any spatial smoothing in our inference approach. Such regularization is not required to approach the target model when the assumed elastic structure is the true one (Fig. S20). Actually, the roughness of the estimates without $\mathbf{C}_p$ is directly related to the amplitude of the assumed observational errors ($\mathbf{C}_d$). Here, we assume conservative values for the observational error, this error being slightly underestimated for some observations (the maximum noise amplitudes reaching ∼10 per cent of the displacement amplitude for 6 per cent for the observational errors). There is thus no room in $\mathbf{C}_d$ to encapsulate any other type of bias, such as the epistemic uncertainties, and the predictions do require a rough model to reproduce the observations. If $\mathbf{C}_d$ is artificially increased so that its amplitude becomes slightly larger than $\mathbf{C}_p$, the inferred mean model becomes smoother but remains far from the target (Fig. S23), especially on side B.

5 DISCUSSION AND CONCLUSION

The San Andreas Fault system (SAF, CA, USA) is a well-instrumented natural example to observe 3-D heterogeneities. Many segments of the SAF show sharp across fault contrasts in rock properties (e.g. McGuire & Ben-Zion 2005; Lee *et al.* 2014; Fang *et al.* 2016; Share & Ben-Zion 2016; Qiu *et al.* 2017; Share & Ben-Zion 2018). Low-velocity zones have been observed around many segments (e.g. Li *et al.* 2004; McGuire & Ben-Zion 2005; Lewis *et al.* 2005; Lewis & Ben-Zion 2010; Qiu *et al.* 2017; Rempe *et al.* 2013). Large along strike variations in material properties are observed as well (e.g. Zhao *et al.* 2010; Allam *et al.* 2014; Lee *et al.* 2014; Shaw *et al.* 2015). The 3-D heterogeneity of material properties of the crust around the SAF is not an isolated example, this characteristic being shared by crustal faults in general.

Heterogeneities in the crustal structure influence earthquake initiation, rupture propagation and aseismic phenomena (e.g. Masterlark *et al.* 2001; Ampuero & Ben-Zion 2008; Brietzke *et al.* 2009; Huang *et al.* 2014; Williams & Wallace 2015; Weng *et al.* 2016; Barnes *et al.* 2020). Because of the limitations of our observations, our knowledge of these heterogeneities comes with intrinsic (epistemic) uncertainties. This uncertain 3-D variability in turn biases our estimates of the seismic source (e.g. Wald & Graves 2001; Zhao *et al.* 2004; Hsu *et al.* 2006; Barbot *et al.* 2008; Hartzell *et al.* 2010; Trasatti *et al.* 2011; Gallovič *et al.* 2015; Gombert *et al.* 2017; Williams & Wallace 2018). In this study, we investigate the impact of uncertain 3-D heterogeneities in elastic parameters on slip estimates inferred from static observations. We build on the method originally proposed by Duputel *et al.* (2014) and based on perturbation theory as applied to 2.5-D infinitely long fault and 3-D finite-fault toy models to show that accounting for epistemic uncertainties allows us to restrict or cancel out the impact of crustal 3-D heterogeneity in source estimates.

Many authors have shown that assuming realistic 3-D crustal structures would lead to more accurate source estimates (e.g. Cattin *et al.* 1999; Masterlark 2003; Hsu *et al.* 2006; Gallovič *et al.* 2015; Wang & Fialko 2018). The estimation of displacements in 3-D crustal structures relies on the use of 3-D numerical simulations, that are more computationally demanding than semi-analytical methods for homogeneous or layered crusts. The use of numerical simulations for 3-D heterogeneous crust will probably become more efficient with the popularization of user-friendly packages (e.g. Aagaard *et al.* 2013; Gharti *et al.* 2019) and computational power.

However, we demonstrate that if the assumed realistic crustal structure does not exactly replicate the reality (which is probably always the case), epistemic uncertainties can lead to large biases in inferred slip distributions. Similar results where found by Graves & Wald (2001), who infer valid source models with a correct 3-D crustal structure, but biased results when assuming an inaccurate 3-D crust. Because of the trade-off between model parameters, inaccuracies in assumed structure might cause unrealistic changes in source estimates if epistemic uncertainties are not introduced (Fig. 9, similarly to other types of uncertainties, Ragon *et al.* 2019). With any assumed crustal structure, accounting for related uncertainties yields more robust and accurate results.

We also show that the most accurate results are obtained when accounting for uncertainties while assuming a realistic Earth interior (or as realistic as possible regarding the limitations of the observations). Not surprisingly, the closer our model is to the true structure, the most accurate our estimates will be.

Our approach to estimating $\mathbf{C}_p$ for 3-D heterogeneities of the crust also relies on 3-D numerical simulation. As suggested by Duputel *et al.* (2014), our approach consists of assessing the impact of small variations of mechanical properties for various domains of the crust. These domains are defined in terms of known (or assumed) heterogeneities of the local crustal structure. Calculating the epistemic uncertainties matrix only requires one additional estimate of the surface deformation per domain.

The calculation of $\mathbf{C}_p$ can be simplified for 3-D crustal structures which comprise horizontal stratifications. We showed that uncertainties deriving from both horizontal and vertical variations of crustal properties can be approximated by independent estimates of the sensitivity of the Green's functions to vertical variations or horizontal variations. For instance, we show that if the assumed crustal structure is layered and contains a vertical heterogeneity, we can derive uncertainties (although less efficiently) separately from the layers and from the vertical heterogeneity in a homogeneous

medium, rather than from six distinct domains. This former approach could lower the computational cost for continental events, as fewer numerical simulations would be necessary.

The crust is heterogeneous at all scales (e.g. Wu & Aki 1985; Levander & Holliger 1992; Dolan *et al.* 1998; Marsan & Bean 2003), and thus domains of homogeneous crustal properties, assumed to simplify 3-D simulations, probably present some intrinsic heterogeneity. We show with our 2.5-D toy models that if the assumed structure is closer to the reality than expected, accounting for uncertainties is still efficient. Our approach to account for uncertainties will thus be viable to include intrinsic domain heterogeneity.

If no or few data are sensitive to a heterogeneity in mechanical properties of the crust, then source estimates will not be impacted. For toy models in which damage zones are neglected, estimated slip models are correct if few data are located within the damage zone, but are biased if a certain amount is affected. These tests have been made with an unrealistic velocity contrast of 0.5, which would probably be lower for large earthquakes (e.g. Mitchell & Faulkner 2009; Faulkner *et al.* 2010; Savage & Brodsky 2011; Mitchell & Faulkner 2012), and few observations would be located within 1–2 km of the fault. However, accounting for damaged zones becomes necessary if a non-negligible fraction of observations is disturbed: such as with improved near-fault coverage (i.e. with optical images correlation, e.g. Avouac *et al.* 2006; Leprince *et al.* 2007; Milliner *et al.* 2015; Marchandon *et al.* 2018).

In this study, we investigate the impact of crustal 3-D structural complexity on slip estimates inferred from geodetic observations and analyse an approach to mitigate the impact of imperfect knowledge of this complexity on estimates of subsurface fault slip. We demonstrate that accounting for epistemic uncertainties within the inference procedure is viable and effective. We use a small perturbation approach as applied to 2.5-D infinitely long fault and 3-D finite-fault toy models to show that, when the assumed structure does not replicate the reality, only accounting for epistemic uncertainty allows us to reliably estimate the slip distribution. We have focused here on coseismic models constrained by geodetic data. The issues and approaches we have discussed here apply equally to models that incorporate seismic data and to models of post-seimic or interseismic processes.

This paper aims to pave the way towards uncertainty acknowledgement for complex crustal structures characterized from observations. The presented approach can be used for any 3-D crustal structure than can be discretized into domains of heterogeneous material properties and shapes, such as element-sets if using finite element methods. For any domain, the proposed approach would only require the additional computation of Green's functions with a different material property. The shape and size of crustal domains will be adapted in function of the observed crustal structure and the available computational power. Our approach can also be used to account for uncertainty in the definition of domain boundaries, which often remain uncertain approximations of the reality, but only at greater computational cost. Similarly, our approach would be only difficultly adapted to continuous variations in crustal properties, because would require an overdiscretization of the crust with homogeneous subregions to approximate the variations, and thus again a drastic increase in computational cost.

ACKNOWLEDGEMENTS

REFERENCES

Aagaard, B.T., Knepley, M.G. & Williams, C.A., 2013. A domain decomposition approach to implementing fault slip in finite-element models of quasi-static and dynamic crustal deformation, *J. geophys. Res.,* **118**(6), 3059–3079.

Agostinetti, N.P., Giacomuzzi, G. & Chiarabba, C., 2020. Across-fault velocity gradients and slip behavior of the San Andreas Fault Near Parkfield, *Geophys. Res. Lett.,* **47**(1), e2019GL084480, doi:10.1029/2019GL084480.

Allam, A.A. & Ben-Zion, Y., 2012. Seismic velocity structures in the southern California plate-boundary environment from double-difference tomography, *J. geophys. Int.,* **190**(2), 1181–1196.

Allam, A.A., Ben-Zion, Y., Kurzon, I. & Vernon, F., 2014. Seismic velocity structure in the Hot Springs and Trifurcation areas of the San Jacinto fault zone, California, from double-difference tomography, *J. geophys. Int.,* **198**(2), 978–999.

Ampuero, J.-P. & Ben-Zion, Y., 2008. Cracks, pulses and macroscopic asymmetry of dynamic rupture on a bimaterial interface with velocity-weakening friction, *J. geophys. Int.,* **173**(2), 674–692.

Aochi, H. & Madariaga, R., 2003. The 1999 Izmit, Turkey, earthquake: nonplanar fault structure, dynamic rupture process, and strong ground motion, *Bull. seism. Soc. Am.,* **93**(3), 1249–1266.

Avouac, J.-P., Ayoub, F., Leprince, S., Konca, O. & Helmberger, D.V., 2006. The 2005, Mw 7.6 Kashmir earthquake: sub-pixel correlation of ASTER images and seismic waveforms analysis, *Earth planet. Sci. Lett.,* **249**(3), 514–528.

Barbot, S., Fialko, Y. & Sandwell, D., 2008. Effect of a compliant fault zone on the inferred earthquake slip distribution, *J. geophys. Res.,* **113**(B6), B06404.

Barnes, P.M., *et al.*, 2020. Slow slip source characterized by lithological and geometric heterogeneity, *Sci. Adv.,* **6**(13), eaay3314.

Ben-Zion, Y. & Andrews, D.J., 1998. Properties and implications of dynamic rupture along a material interface, *Bull. seism. Soc. Am.,* **88**(4), 1085–1094.

Ben-Zion, Y. & Sammis, C.G., 2003. Characterization of fault zones, *Pure appl. Geophys.,* **160**(3–4), 677–715.

Beresnev, I.A., 2003. Uncertainties in finite-fault slip inversions: to what extent to believe? (A critical review), *Bull. seism. Soc. Am.,* **93**(6), 2445–2458.

Bouchon, M., Campillo, M. & Cotton, F., 1998. Stress field associated with the rupture of the 1992 Landers, California, earthquake and its implications concerning the fault strength at the onset of the earthquake, *J. geophys. Res.,* **103**(B9), 21 091–21 097.

Brietzke, G.B., Cochard, A. & Igel, H., 2009. Importance of bimaterial interfaces for earthquake dynamics and strong ground motion, *J. geophys. Int.,* **178**(2), 921–938.

Bulut, F., Ben-Zion, Y. & Bohnhoff, M., 2012. Evidence for a bimaterial interface along the Mudurnu segment of the North Anatolian Fault Zone from polarization analysis of P waves, *Earth planet. Sci. Lett.,* **327–328**, 17–22.

Candela, T., Renard, F., Klinger, Y., Mair, K., Schmittbuhl, J. & Brodsky, E.E., 2012. Roughness of fault surfaces over nine decades of length scales, *J. geophys. Res.,* **117**(B8), B08409.

Cappa, F., Perrin, C., Manighetti, I. & Delor, E., 2014. Off-fault long-term damage: a condition to account for generic, triangular earthquake slip profiles, *Geochem. Geophys. Geosyst.,* **15**(4), 1476–1493.

Cattin, R., Briole, P., Lyon-Caen, H., Bernard, P. & Pinettes, P., 1999. Effects of superficial layers on coseismic displacements for a dip-slip fault and geophysical implications, *J. geophys. Int.,* **137**(1), 149–158.

Cervelli, P., Kenner, S. & Segall, P., 1999. Correction to 'Dislocations in inhomogeneous media via a moduli perturbation approach: General formulation and two-dimensional solutions' by Yijun Du, Paul Segall, and Huajian Gao, *J. geophys. Res.,* **104**(B10), 23 271–23 277.

Diao, F., Wang, R., Aochi, H., Walter, T.R., Zhang, Y., Zheng, Y. & Xiong, X., 2016. Rapid kinematic finite-fault inversion for an Mw 7+ scenario earthquake in the Marmara Sea: an uncertainty study, *J. geophys. Int.,* **204**(2), 813–824.

Dolan, S.S., Bean, C.J. & Riollet, B., 1998. The broad-band fractal nature of heterogeneity in the upper crust from petrophysical logs, *J. geophys. Int.,* **132**(3), 489–507.

Du, Y., Segall, P. & Gao, H., 1994. Dislocations in inhomogeneous media via a moduli perturbation approach: general formulation and two-dimensional solutions, *J. geophys. Res.,* **99**(B7), 13 767–13 779.

Duputel, Z., Rivera, L., Fukahata, Y. & Kanamori, H., 2012. Uncertainty estimations for seismic source inversions, *J. geophys. Int.,* **190**(2), 1243–1256.

Duputel, Z., Agram, P.S., Simons, M., Minson, S.E. & Beck, J.L., 2014. Accounting for prediction uncertainty when inferring subsurface fault slip, *J. geophys. Int.,* **197**(1), 464–482.

Fang, H., Zhang, H., Yao, H., Allam, A., Zigone, D., Ben-Zion, Y., Thurber, C. & van der Hilst, R.D., 2016. A new algorithm for three-dimensional joint inversion of body wave and surface wave data and its application to the Southern California plate boundary region, *J. geophys. Res.,* **121**(5), 3557–3569.

Faulkner, D.R., Lewis, A.C. & Rutter, E.H., 2003. On the internal structure and mechanics of large strike-slip fault zones: field observations of the Carboneras fault in southeastern Spain, *Tectonophysics,* **367**(3), 235–251.

Faulkner, D.R., Mitchell, T.M., Healy, D. & Heap, M.J., 2006. Slip on 'weak' faults by the rotation of regional stress in the fracture damage zone, *Nature,* **444**(7121), 922–925.

Faulkner, D.R., Jackson, C.A.L., Lunn, R.J., Schlische, R.W., Shipton, Z.K., Wibberley, C.A.J. & Withjack, M.O., 2010. A review of recent developments concerning the structure, mechanics and fluid flow properties of fault zones, *J. Struct. Geol.,* **32**(11), 1557–1575.

Gabriel, A.-A., Ampuero, J.-P., Dalguer, L.A. & Mai, P.M., 2013. Source properties of dynamic rupture pulses with off-fault plasticity, *J. geophys. Res.,* **118**(8), 4117–4126.

Gallovič, F., Imperatori, W. & Mai, P.M., 2015. Effects of three-dimensional crustal structure and smoothing constraint on earthquake slip inversions: case study of the Mw6.3 2009 L'Aquila earthquake, *J. geophys. Res.,* **120**(1), 2014JB011650.

Gharti, H.N., Langer, L. & Tromp, J., 2019. Spectral-infinite-element simulations of coseismic and postearthquake deformation, *J. geophys. Int.,* **216**(2), 1364–1393.

Gombert, B., Duputel, Z., Jolivet, R., Doubre, C., Rivera, L. & Simons, M., 2017. Revisiting the 1992 Landers earthquake: a Bayesian exploration of co-seismic slip and off-fault damage, *J. geophys. Int.,* **212**(2), 839–852

Graves, R.W. & Wald, D.J., 2001. Resolution analysis of finite fault source inversion using one- and three-dimensional Green's functions: 1. Strong motions, *J. geophys. Res,* **106**(B5), 8745–8766.

Gudmundsson, A., 2007. Infrastructure and evolution of ocean-ridge discontinuities in Iceland, *J. Geodyn.,* **43**(1), 6–29.

Hallo, M. & Gallovič, F., 2016. Fast and cheap approximation of Green function uncertainty for waveform-based earthquake source inversions, *J. geophys. Int.,* **207**(2), 1012–1029.

Hallo, M. & Gallovič, F., 2020. Bayesian self-adapting fault slip inversion with Green's functions uncertainty and application on the 2016 Mw7.1 Kumamoto earthquake, *J. geophys. Res.,* **125**(3), e2019JB018703.

Hartzell, S., Liu, P., Mendoza, C., Ji, C. & Larson, K.M., 2007. Stability and uncertainty of finite-fault slip inversions: application to the 2004 Parkfield, California, Earthquake, *Bull. seism. Soc. Am.,* **97**(6), 1911–1934.

Hartzell, S., Harmsen, S. & Frankel, A., 2010. Effects of 3D random correlated velocity perturbations on predicted ground motions, *Bull. seism. Soc. Am.,* **100**(4), 1415–1426.

He, Y.-M., Wang, W.-M. & Yao, Z.-X., 2003. Static deformation due to shear and tensile faults in a layered half-space, *Bull. seism. Soc. Am.,* **93**(5), 2253–2263.

Hearn, E.H. & Bürgmann, R., 2005. The effect of elastic layering on inversions of GPS data for coseismic slip and resulting stress changes: strike-slip earthquakes, *Bull. seism. Soc. Am.,* **95**(5), 1637–1653.

Hsu, Y.-J., *et al.*, 2006. Frictional afterslip following the 2005 Nias-Simeulue Earthquake, Sumatra, *Science,* **312**(5782), 1921–1926.

Hsu, Y.-J., Simons, M., Williams, C. & Casarotti, E., 2011. Three-dimensional FEM derived elastic Green's functions for the coseismic deformation of the 2005 Mw 8.7 Nias-Simeulue, Sumatra earthquake, *Geochem. Geophys. Geosyst.,* **12**(7), Q07013.

Huang, Y. & Ampuero, J.-P., 2011. Pulse-like ruptures induced by low-velocity fault zones, *J. geophys. Res.,* **116**(B12), doi:10.1029/2011JB008684.

Huang, Y., Ampuero, J.-P. & Helmberger, D.V., 2014. Earthquake ruptures modulated by waves in damaged fault zones, *J. geophys. Res.,* **119**(4), 3133–3154.

Jiang, J. & Simons, M., 2016. Probabilistic imaging of tsunamigenic seafloor deformation during the 2011 Tohoku-oki Earthquake, *J. geophys. Res.,* **121**(12), 9050–9076

Jolivet, R., Bürgmann, R. & Houlié, N., 2009. Geodetic exploration of the elastic properties across and within the northern San Andreas Fault zone, *Earth planet. Sci. Lett.,* **288**(1), 126–131.

Jolivet, R., *et al.*, 2014. The 2013 Mw 7.7 Balochistan earthquake: seismic potential of an accretionary wedge, *Bull. seism. Soc. Am.,* **104**(2), 1020–1030.

Jovanovich, D.B., Husseini, M.I. & Chinnery, M.A., 1974. Elastic dislocations in a layered half-space – I. Basic theory and numerical methods, *J. geophys. Int.,* **39**(2), 205–217.

Kahraman, M., *et al.*, 2015. Crustal-scale shear zones and heterogeneous structure beneath the North Anatolian Fault Zone, Turkey, revealed by a high-density seismometer array, *Earth planet. Sci. Lett.,* **430**, 129–139.

King, G. & Nabelek, J., 1985. Role of Fault Bends in the Initiation and Termination of Earthquake Rupture, *Science,* **228**(4702), 984–987.

Komatitsch, D. & Tromp, J., 2002. Spectral-element simulations of global seismic wave propagation—I. Validation, *J. geophys. Int.,* **149**(2), 390–412.

Langer, L., Gharti, H.N. & Tromp, J., 2019. Impact of topography and three-dimensional heterogeneity on coseismic deformation, *J. geophys. Int.,* **217**(2), 866–878.

Langer, L., Ragon, T., Sladen, A. & Tromp, J., 2020. Impact of topography on earthquake static slip inversions, Preprint, EarthArXiv, doi:10.31223/osf.io/nsbx3.

Lee, E.-J., Chen, P., Jordan, T.H., Maechling, P.B., Denolle, M.A.M. & Beroza, G.C., 2014. Full-3-D tomography for crustal structure in Southern California based on the scattering-integral and the adjoint-wavefield methods, *J. geophys. Res.,* **119**(8), 6421–6451.

Lee, S.-J., Ma, K.-F. & Chen, H.-W., 2006. Effects of fault geometry and slip style on near-fault static displacements caused by the 1999 Chi-Chi, Taiwan earthquake, *Earth planet. Sci. Lett.,* **241**(1–2), 336–350.

Leprince, S., Barbot, S., Ayoub, F. & Avouac, J.-P., 2007. Automatic and precise orthorectification, coregistration, and subpixel correlation of satellite images, application to ground deformation measurements, *IEEE Trans. Geosci. Rem. Sens.,* **45**(6), 1529–1558.

Levander, A.R. & Holliger, K., 1992. Small-scale heterogeneity and large-scale velocity structure of the continental crust, *J. geophys. Res.,* **97**(B6), 8797–8804.

Lewis, M.A. & Ben-Zion, Y., 2010. Diversity of fault zone damage and trapping structures in the Parkfield section of the San Andreas Fault from comprehensive analysis of near fault seismograms, *J. geophys. Int.,* **183**(3), 1579–1595.

Lewis, M.A., Peng, Z., Ben-Zion, Y. & Vernon, F.L., 2005. Shallow seismic trapping structure in the San Jacinto fault zone near Anza, California, *J. geophys. Int.,* **162**(3), 867–881.

Li, Y.-G., Vidale, J.E. & Cochran, E.S., 2004. Low-velocity damaged structure of the San Andreas Fault at Parkfield from fault zone trapped waves, *Geophys. Res. Lett.,* **31**(12), doi:10.1029/2003GL019044.

Liu, P. & Archuleta, R.J., 2004. A new nonlinear finite fault inversion with three-dimensional Green's functions: application to the 1989 Loma Prieta, California, earthquake, *J. geophys. Res.,* **109**(B2), doi:10.1029/2003JB002625.

Mahrer, K.D., 1981. Strike-slip faulting in a bi-directionally varying crust, *Bull. seism. Soc. Am.,* **71**(2), 391–404.

Mai, P.M., *et al.*, 2016. The earthquake-source inversion validation (SIV) project, *Seismol. Res. Lett.,* **87**(3), 690–708.

Marchandon, M., Vergnolle, M., Sudhaus, H. & Cavalié, O., 2018. Fault geometry and slip distribution at depth of the 1997 Mw 7.2 Zirkuh earthquake: contribution of near-field displacement data, *J. geophys. Res.,* **123**(2), 1904–1924.

Marsan, D. & Bean, C., 2003. Multifractal modeling and analyses of crustal heterogeneity, in *Heterogeneity in the Crust and Upper Mantle: Nature, Scaling, and Seismic Properties,* pp. 207–236, eds Goff, J.A. & Holliger, K., Springer US.

Masterlark, T., 2003. Finite element model predictions of static deformation from dislocation sources in a subduction zone: sensitivities to homogeneous, isotropic, Poisson-solid, and half-space assumptions, *J. geophys. Res.,* **108**(B11), doi:10.1029/2002JB002296.

Masterlark, T., DeMets, C., Wang, H.F., Sánchez, O. & Stock, J., 2001. Homogeneous vs heterogeneous subduction zone models: coseismic and postseismic deformation, *Geophys. Res. Lett.,* **28**(21), 4047–4050.

Materna, K. & Bürgmann, R., 2016. Contrasts in compliant fault zone properties inferred from geodetic measurements in the San Francisco Bay area, *J. geophys. Res.,* **121**(9), 6916–6931.

McGuire, J. & Ben-Zion, Y., 2005. High-resolution imaging of the Bear Valley section of the San Andreas fault at seismogenic depths with fault-zone head waves and relocated seismicity, *J. geophys. Int.,* **163**(1), 152–164.

Menke, W., 2012. *Geophysical Data Analysis: Discrete Inverse Theory,* Academic Press.

Milliner, C.W.D., Dolan, J.F., Hollingsworth, J., Leprince, S., Ayoub, F. & Sammis, C.G., 2015. Quantifying near-field and off-fault deformation patterns of the 1992 Mw 7.3 Landers earthquake, *Geochem. Geophys. Geosyst.,* **16**(5), 1577–1598.

Minson, S.E., Simons, M. & Beck, J.L., 2013. Bayesian inversion for finite fault earthquake source models I – theory and algorithm, *J. geophys. Int.,* **194**(3), 1701–1726.

Minson, S.E., *et al.*, 2014. Bayesian inversion for finite fault earthquake source models – II: the 2011 great Tohoku-oki, Japan earthquake, *J. geophys. Int.,* **198**(2), 922–940.

Mitchell, T.M. & Faulkner, D.R., 2009. The nature and origin of off-fault damage surrounding strike-slip fault zones with a wide range of displacements: a field study from the Atacama fault system, northern Chile, *J. Struct. Geol.,* **31**(8), 802–816.

Mitchell, T.M. & Faulkner, D.R., 2012. Towards quantifying the matrix permeability of fault damage zones in low porosity rocks, *Earth planet. Sci. Lett.,* **339–340**, 24–31.

Moreno, M.S., Bolte, J., Klotz, J. & Melnick, D., 2009. Impact of megathrust geometry on inversion of coseismic slip from geodetic data: application to the 1960 Chile earthquake, *Geophys. Res. Lett.,* **36**(16), L16310.

Najdahmadi, B., Bohnhoff, M. & Ben-Zion, Y., 2016. Bimaterial interfaces at the Karadere segment of the North Anatolian Fault, northwestern Turkey, *J. geophys. Res.,* **121**(2), 931–950.

Ozakin, Y., Ben-Zion, Y., Aktar, M., Karabulut, H. & Peng, Z., 2012. Velocity contrast across the 1944 rupture zone of the North Anatolian fault east of Ismetpasa from analysis of teleseismic arrivals, *Geophys. Res. Lett.,* **39**(8), doi:10.1029/2012GL051426.

Pan, E., 1999. Green's functions in layered poroelastic half-spaces, *Int. J. Numer. Anal. Method. Geomech.,* **23**(13), 1631–1653.

Parker, J., Lyzenga, G., Norton, C., Zuffada, C., Glasscoe, M., Lou, J. & Donnellan, A., 2008. Geophysical finite-element simulation tool (GeoFEST): algorithms and validation for quasistatic regional faulted crust problems, *Pure appl. Geophys.,* **165**(3), 497–521.

Perrin, C., Manighetti, I., Ampuero, J.-P., Cappa, F. & Gaudemer, Y., 2016a. Location of largest earthquake slip and fast rupture controlled by along-strike change in fault structural maturity due to fault growth, *J. geophys. Res.,* **121**(5), 3666–3685.

Perrin, C., Manighetti, I. & Gaudemer, Y., 2016b. Off-fault tip splay networks: a genetic and generic property of faults indicative of their long-term propagation, *Compt. Rend. Geosci.,* **348**(1), 52–60.

Pichon, X.L., Kreemer, C. & Chamot-Rooke, N., 2005. Asymmetry in elastic properties and the evolution of large continental strike-slip faults, *J. geophys. Res.,* **110**(B3), doi:10.1029/2004JB003343.

Pizzi, A., Di Domenica, A., Gallovič, F., Luzi, L. & Puglia, R., 2017. Fault segmentation as constraint to the occurrence of the main shocks of the 2016 Central Italy seismic sequence, *Tectonics,* **36**(11), 2370–2387.

Qiu, H., Ben-Zion, Y., Ross, Z.E., Share, P.-E. & Vernon, F.L., 2017. Internal structure of the San Jacinto fault zone at Jackass Flat from data recorded by a dense linear array, *J. geophys. Int.,* **209**(3), 1369–1388.

Ragon, T., Sladen, A. & Simons, M., 2018. Accounting for uncertain fault geometry in earthquake source inversions – I: theory and simplified application, *J. geophys. Int.,* **214**(2), 1174–1190.

Ragon, T., Sladen, A. & Simons, M., 2019. Accounting for uncertain fault geometry in earthquake source inversions – II: application to the Mw 6.2 Amatrice earthquake, central Italy, *J. geophys. Int.,* **218**(1), 689–707.

Razafindrakoto, H.N.T. & Mai, P.M., 2014. Uncertainty in earthquake source imaging due to variations in source time function and earth structure, *Bull. seism. Soc. Am.,* **104**(2), 855–874.

Reinoza, C., Jouanne, F., Audemard, F.A., Schmitz, M. & Beck, C., 2015. Geodetic exploration of strain along the El Pilar Fault in northeastern Venezuela, *J. geophys. Res.,* **120**(3), 1993–2013.

Rempe, M., Mitchell, T., Renner, J., Nippress, S., Ben-Zion, Y. & Rockwell, T., 2013. Damage and seismic velocity structure of pulverized rocks near the San Andreas Fault, *J. geophys. Res.,* **118**(6), 2813–2831.

Rybicki, K., 1971. The elastic residual field of a very long strike-slip fault in the presence of a discontinuity, *Bull. seism. Soc. Am.,* **61**(1), 79–92.

Rybicki, K. & Kasahara, K., 1977. A strike-slip fault in a laterally inhomogeneous medium, *Tectonophysics,* **42**(2), 127–138.

Sagy, A. & Brodsky, E.E., 2009. Geometric and rheological asperities in an exposed fault zone, *J. geophys. Res.,* **114**(B2), doi:10.1029/2008JB005701.

Sammis, C.G., Rosakis, A.J. & Bhat, H.S., 2009. Effects of off-fault damage on earthquake rupture propagation: experimental studies, *Pure appl. Geophys.,* **166**(10), 1629–1648.

Sato, R., 1971. Crustal deformation due to dislocation in a multi-layered medium, *J. Phys. Earth,* **19**(1), 31–46.

Sato, R. & Matsu'ura, M., 1973. Static deformations due to the fault spreading over several layers in a multi-layered medium, *J. Phys. Earth,* **21**(3), 227–249.

Savage, H.M. & Brodsky, E.E., 2011. Collateral damage: evolution with displacement of fracture distribution and secondary fault strands in fault damage zones, *J. geophys. Res.,* **116**(B3), doi:10.1029/2010JB007665.

Savage, J.C., 1987. Effect of crustal layering upon dislocation modeling, *J. geophys. Res.,* **92**(B10), 10 595–10 600.

Schmalzle, G., Dixon, T., Malservisi, R. & Govers, R., 2006. Strain accumulation across the Carrizo segment of the San Andreas Fault, California: impact of laterally varying crustal properties, *J. geophys. Res.,* **111**(B5).

Segall, P., 2010. *Earthquake and Volcano Deformation,* Princeton Univ. Press.

Share, P.-E. & Ben-Zion, Y., 2016. Bimaterial interfaces in the south San Andreas Fault with opposite velocity contrasts NW and SE from San Gorgonio Pass, *Geophys. Res. Lett.,* **43**(20), 10 680–10 687.

Share, P.-E. & Ben-Zion, Y., 2018. A bimaterial interface along the Northern San Jacinto Fault through Cajon Pass, *Geophys. Res. Lett.,* **45**(21), 11 622–11 631.

Shaw, J.H., *et al.*, 2015. Unified Structural Representation of the southern California crust and upper mantle, *Earth planet. Sci. Lett.,* **415,** 1–15.

Simons, M., Fialko, Y. & Rivera, L., 2002. Coseismic deformation from the 1999 Mw 7.1 Hector Mine, California, earthquake as inferred from InSAR and GPS observations, *Bull. seism. Soc. Am.,* **92**(4), 1390–1402.

Spudich, P. & Olsen, K.B., 2001. Fault zone amplified waves as a possible seismic hazard along the Calaveras Fault in central California, *Geophys. Res. Lett.,* **28**(13), 2533–2536.

Tarantola, A., 2005. *Inverse Problem Theory and Methods for Model Parameter Estimation, Other Titles in Applied Mathematics,* Society for Industrial and Applied Mathematics.

Trasatti, E., Kyriakopoulos, C. & Chini, M., 2011. Finite element inversion of DInSAR data from the Mw 6.3 L'Aquila earthquake, 2009 (Italy), *Geophys. Res. Lett.,* **38**(8), L08306.

Tromp, J., Tape, C. & Liu, Q., 2005. Seismic tomography, adjoint methods, time reversal and banana-doughnut kernels, *J. geophys. Int.,* **160**(1), 195–216.

Virieux, J., 1986. P-SV wave propagation in heterogeneous media: velocity-stress finite-difference method, *Geophysics,* **51**(4), 889–901.

Wald, D.J. & Graves, R.W., 2001. Resolution analysis of finite fault source inversion using one- and three-dimensional Green's functions: 2. Combining seismic and geodetic data, *J. geophys. Res.,* **106**(B5), 8767–8788.

Wang, K. & Fialko, Y., 2018. Observations and modeling of coseismic and postseismic deformation due to the 2015 Mw 7.8 Gorkha (Nepal) earthquake, *J. geophys. Res.,* **123**(1), 761–779.

Wei, S., *et al.*, 2011. Superficial simplicity of the 2010 El Mayor-Cucapah earthquake of Baja California in Mexico, *Nat. Geosci.,* **4**(9), 615–618.

Weng, H., Yang, H., Zhang, Z. & Chen, X., 2016. Earthquake rupture extents and coseismic slips promoted by damaged fault zones, *J. geophys. Res.,* **121**(6), 4446–4457.

Williams, C.A. & Wallace, L.M., 2015. Effects of material property variations on slip estimates for subduction interface slow-slip events, *Geophys. Res. Lett.,* **42**(4), 1113–1121.

Williams, C.A. & Wallace, L.M., 2018. The impact of realistic elastic properties on inversions of shallow subduction interface slow slip events using seafloor geodetic data, *Geophys. Res. Lett.,* **45**(15), 7462–7470.

Wilson, J.E., Chester, J.S. & Chester, F.M., 2003. Microfracture analysis of fault growth and wear processes, Punchbowl Fault, San Andreas system, California, *J. Struct. Geol.,* **25**(11), 1855–1873.

Wu, R.-S. & Aki, K., 1985. The fractal nature of the inhomogeneities in the lithosphere evidenced from seismic wave scattering, *Pure appl. Geophys.,* **123**(6), 805–818.

Yagi, Y. & Fukahata, Y., 2008. Importance of covariance components in inversion analyses of densely sampled observed data: an application to waveform data inversion for seismic source processes, *J. geophys. Int.,* **175**(1), 215–221.

Yagi, Y. & Fukahata, Y., 2011. Introduction of uncertainty of Green's function into waveform inversion for seismic source processes, *J. geophys. Int.,* **186**(2), 711–720.

Yolsal-Çevikbilen, S., Biryol, C.B., Beck, S., Zandt, G., Taymaz, T., Adiyaman, H.E. & Özacar, A.A., 2012. 3-D crustal structure along the North Anatolian Fault Zone in north-central Anatolia revealed by local earthquake tomography, *J. geophys. Int.,* **188**(3), 819–849.

Zeng, X., *et al.*, 2016. 3-D P- and S-wave velocity structure and low-frequency earthquake locations in the Parkfield, California region, *J. geophys. Int.,* **206**(3), 1574–1585.

Zhang, P., Slemmons, D.B. & Mao, F., 1991. Geometric pattern, rupture termination and fault segmentation of the Dixie Valley–Pleasant Valley active normal fault system, Nevada, U.S.A., *J. Struct. Geol.,* **13**(2), 165–176.

Zhao, P., Peng, Z., Shi, Z., Lewis, M.A. & Ben-Zion, Y., 2010. Variations of the velocity contrast and rupture properties of M6 earthquakes along the Parkfield section of the San Andreas fault, *J. geophys. Int.,* **180**(2), 765–780.

Zhao, S., Müller, R.D., Takahashi, Y. & Kaneda, Y., 2004. 3-D finite-element modelling of deformation and stress associated with faulting: effect of inhomogeneous crustal structures, *J. geophys. Int.,* **157**(2), 629–644.

Zhu, L. & Rivera, L.A., 2002. A note on the dynamic and static displacements from a point source in multilayered media, *J. geophys. Int.,* **148**(3), 619–627.

Zielke, O., Galis, M. & Mai, P.M., 2017. Fault roughness and strength heterogeneity control earthquake size and stress drop, *Geophys. Res. Lett.,* **44**, 777–783.

SUPPORTING INFORMATION

Supplementary data are available at *GJI* online.

Figure S1 Illustration of the FEM domain and mesh.

Figure S2 Comparison between FEM simulated surface displacements and approximate analytical displacements for an infinite strike slip fault embedded in an elastic structure composed of two layers above half-space with a lateral heterogeneity (see setup in Fig. A1 and Appendix A4).

Figure S3 Comparison of the Green's functions derived from the approximate analytical solution or from a simulation with the domain described in Fig. S1. In this case, the infinite strike slip fault is embedded in an elastic structure composed of two layers above half space with a lateral heterogeneity (see setup in Fig. A1 and Appendix A4).

Figure S4 Comparisons between target predictions (observations) and predictions with and without accounting for $\mathbf{C}_p$, for an infinite strike slip fault bounding two media of shear moduli μ_1 and μ_2. The target predictions are calculated assuming true Green's functions, while the dashed curves are calculated assuming an homogeneous crustal structure. The uncertainty associated with each curve is in a similar colour. The uncertainty of the target predictions contains $\mathbf{C}_p$. The location of the fault surface rupture is shown with a grey vertical line. The target slip is a uniform slip distribution of 10 m in amplitude.

Figure S5 Variation of the surface displacement (Green's functions) with shear modulus value, for a vertical strike-slip fault bounding two media of shear moduli μ_1 and μ_2. μ_1 (left-hand side of the fault, data from 0 to 50 km) is held fixed and μ_2 (right-hand side) varies. The surface displacement is calculated perpendicularly to the fault (the fault being at 50 km) for a strike slip of 1 m on the shallowest subfault (top panel), at intermediate depth (middle panel) or for the deepest subfault (bottom panel).

Figure S6 Same as Fig.S4, but with the target predictions calculated with a non-uniform target slip distribution, and with correlated noise added.

Figure S7 Comparisons between target predictions (observations) and predictions with and without accounting for $\mathbf{C}_p$, for an infinite strike slip fault embedded in an heterogeneous media, composed of two layers over a half-space and a vertical heterogeneity. The target predictions are calculated assuming true Green's functions, while the dashed curves are calculated assuming an homogeneous crustal structure. The uncertainty associated with each curve is in a similar colour. The uncertainty of the target predictions contains $\mathbf{C}_p$. The location of the fault surface rupture is shown with a grey vertical line. The target slip is a uniform slip distribution of 10 m in amplitude.

Figure S8 Comparisons between target predictions (observations) and predictions with and without accounting for $\mathbf{C}_p$, for an infinite strike slip fault embedded in an heterogeneous media composed of two layers above half space and a vertical heterogeneity, with different velocity gradients on either side of the fault. The target predictions are calculated assuming true Green's functions, while the dashed curves are calculated assuming an homogeneous crustal structure. The uncertainty associated with each curve is in a similar colour. The uncertainty of the target predictions contains $\mathbf{C}_p$. The

location of the fault surface rupture is shown with a grey vertical line. The target slip is a uniform slip distribution of 10 m in amplitude.

Figure S9 Same as Fig. 6, with, in (b) and (c), the crustal structure assumed to be layered, and, in (c), epistemic uncertainties calculated by layers and vertical domains. The assumed layered crustal structure is, for each layer, the average of the true structure.

Figure S10 Same as Fig. 6, with noise added to the synthetic surface displacement. Gaussian noise is combined with spatially correlated noise with a standard deviation being of 6 per cent of the maximum surface displacement.

Figure S11 Same as Fig. S8, with noise added to the synthetic surface displacements (noise realization 1, described in Fig. S10).

Figure S12 Same as Fig. 6, with noise added to the synthetic surface displacement. Gaussian noise is combined with spatially correlated noise with a standard deviation being of 9 per cent of the maximum surface displacement.

Figure S13 Same as Fig. S8, with noise added to the synthetic surface displacements (noise realization 2, described in Fig. S12).

Figure S14 Same as Fig. 7, with noise added to the synthetic surface displacement, and, in (c) epistemic uncertainties calculated for each domain independently.

Figure S15 Same as Fig. 7 but assuming a reverse dip-slip target model. Synthetic surface displacements, Green's functions and uncertainties are FEM-derived.

Figure S16 Comparisons between target predictions (observations) and predictions with and without accounting for $\mathbf{C}_p$, for an infinite dip slip fault embedded in an heterogeneous media composed of two layers above half space and a vertical heterogeneity, with different velocity gradients on either side of the fault. The target predictions are calculated assuming true Green's functions, while the dashed curves are calculated assuming a layered crustal structure. The uncertainty associated with each curve is in a similar colour. The location of the fault surface rupture is shown with a grey vertical line. The target slip is a uniform reverse slip of 10 m in amplitude.

Figure S17 Same as Fig. 8, with a 2-km-wide fault zone.

Figure S18 Comparisons between target predictions (observations) and predictions with and without accounting for $\mathbf{C}_p$, for an infinite strike slip fault embedded in a compliant fault zone. The target predictions are calculated assuming true Green's functions, while the dashed curves are calculated assuming an homogeneous crustal structure. The uncertainty associated with each curve is in a similar colour. The uncertainty of the target predictions contains $\mathbf{C}_p$. The location of the fault surface rupture is shown with a grey vertical line. The target slip is a uniform slip distribution of 10 m in amplitude.

Figure S19 Illustration of the FEM domain and mesh for the 3-D example.

Figure S20 Mean model and standard deviation estimated assuming an homogeneous crust, the true crustal structure being homogeneous too.

Figure S21 Mean dip-slip amplitude for the cases presented in Fig. 9.

Figure S22 Comparison between observed and predicted displacements for the cases presented in Fig. 9. For the vertical surface displacement, the inner values represent the observed amplitudes, and the outer values the predicted amplitudes. The observational and prediction errors are not represented to make the figure easier to read. The average observational error is assumed to be 6 per cent of the displacement. The prediction error depends on whether $\mathbf{C}_p$ is accounted for or not; it averages at 7 per cent without uncertainties, and 25 per cent with $\mathbf{C}_p$.

Figure S23 Mean model and standard deviation estimated for the strike-perpendicular interface case, without accounting for $\mathbf{C}_p$, but with a $\mathbf{C}_d$ proportionally increased so that its amplitude is slightly larger than $\mathbf{C}_p$. In this case, inferred models are particularly far from the target on the side of the fault which is within the region with a varying shear modulus (right-hand side).

Table S1 Grid specifications.

Table S2 Grid specifications for the 3-D example.

Please note: Oxford University Press is not responsible for the content or functionality of any supporting materials supplied by the authors. Any queries (other than missing material) should be directed to the corresponding author for the paper.

APPENDIX A: EXPRESSIONS OF SURFACE DISPLACEMENT FOR A STRIKE-SLIP DISLOCATION IN A 2.5-D MEDIUM

We consider a simple 2.5-D model of a strike-slip fault that extends infinitely along strike. Strike-perpendicular and vertical directions are respectively defined by the $\mathbf{x}_1$ and $\mathbf{x}_2$ axes, the free surface being the $\mathbf{x}_1$, $\mathbf{x}_3$ plane. The displacement on the fault is restricted to the $\mathbf{x}_3$ direction (i.e. along strike direction). Each surface displacement is calculated for a particular data point located at x_1 along the strike-perpendicular direction $\mathbf{x}_1$ (and then for $x_2 = 0$).

A1 Strike-slip fault bounding two media

Following Segall (2010), we can derive the expression of the surface displacement produced by an infinitely long vertical strike-slip fault bounding two media of different shear modulus, μ_1 and μ_2. The slip s on the fault extends from the free surface to depth d. We will refer to displacement $u^{(1)}$ on the side with modulus μ_1, and to displacement $u^{(2)}$ on the side with modulus μ_2.

$$u_v^{(1)}(x_1 < 0, x_2 = 0) = \frac{2s}{\pi} \frac{\mu_2}{\mu_1 + \mu_2} \tan^{-1}\left(\frac{d}{x_1}\right)$$

$$u_v^{(2)}(x_1 > 0, x_2 = 0) = \frac{2s}{\pi} \frac{\mu_1}{\mu_1 + \mu_2} \tan^{-1}\left(\frac{d}{x_1}\right) \qquad \text{(A1)}$$

A2 One-layer above half-space

We first investigate the case of a medium composed of one horizontal layer of thickness h and shear modulus μ_A, overlying a half-space of different shear modulus μ_C. Slip s on the strike-slip fault extends from the free surface to a depth d, with $d \geq h$. We can derive from Rybicki (1971) the expression of the displacement at the free

surface as:

$$u_A(x_1, x_2 = 0) = \frac{s}{\pi} \tan^{-1}\left(\frac{h}{x_1}\right)$$
$$+ \frac{s(1 - K_A)}{\pi}\left[\tan^{-1}\left(\frac{d}{x_1}\right) - \tan^{-1}\left(\frac{h}{x_1}\right)\right]$$
$$+ \frac{s}{\pi}\sum_{m=1}^{+\infty} K_A^m \left[\tan^{-1}\left(\frac{(1 + 2m)h}{x_1}\right)\right.$$
$$+ \tan^{-1}\left(\frac{(1 - 2m)h}{x_1}\right)\right]$$
$$+ \frac{s(1 - K_A)}{\pi}\sum_{m=1}^{+\infty} K_A^m \left[\tan^{-1}\left(\frac{d + 2mh}{x_1}\right)\right.$$
$$\left. - \tan^{-1}\left(\frac{(1 + 2m)h}{x_1}\right)\right],$$

(A2)

$\forall d \geq h$, and defining K_A as:

$$K_A = \frac{\mu_A - \mu_C}{\mu_A + \mu_C}.$$

(A3)

Also note that, if $d \leq h$, the surface displacement become (Rybicki 1971; Segall 2010):

$$u_A(x_1, x_2 = 0) = \frac{s}{\pi}\tan^{-1}\left(\frac{d}{x_1}\right)$$
$$+ \frac{s}{\pi}\sum_{m=1}^{+\infty} K_A^m \left[\tan^{-1}\left(\frac{d + 2mh}{x_1}\right)\right.$$
$$\left. + \tan^{-1}\left(\frac{d - 2mh}{x_1}\right)\right],$$

(A4)

$\forall d \leq h$.

A3 Two layers above half-space

We now consider the case of two layers, of shear moduli μ_1 and μ_2 and thickness h_A and h_B, overlying a half-space of shear modulus μ_3, the slip extending from the free surface to a depth $d \geq h_B \geq h_A$. The slip can be formulated as the sum of two 'one-layer' dislocations, whose resulting displacement has been given in eq. (A.3) (Fig. A1).

We approximate the solution with a moduli perturbation approach (e.g. Du *et al.* 1994; Cervelli *et al.* 1999; Segall 2010). We assume that the surface displacement induced by a dislocation of slip s is equivalent to the superposition of 2 similar dislocations of slip $s/2$ embedded in 2 different structure. A validation of this approximation appears in Section 2.2.2.

We consider a first dislocation in a medium with one layer of thickness h_A and shear modulus μ_A overlying a half-space of shear modulus μ_C, the slip $s/2$ extending from the free surface to a depth $d \geq h_A$. A second dislocation is superposed to the first one, characterized by a slip $s/2$ extending from the free surface to a depth $d \geq h_B \geq h_A$, in a medium with one layer of thickness h_B and shear modulus μ_B overlying a half-space of shear modulus μ_C.

$$u_2(x_1, x_2 = 0) = \frac{1}{2}\left(u_A(x_1, x_2 = 0) + u_B(x_1, x_2 = 0)\right)$$

(A5)

$\forall d \geq h_B \geq h_A$, with $\mu_A \neq \mu_C$, $\mu_B \neq \mu_C$ and defining K_A as

$$K_A = \frac{\mu_A - \mu_C}{\mu_A + \mu_C},$$

(A6)
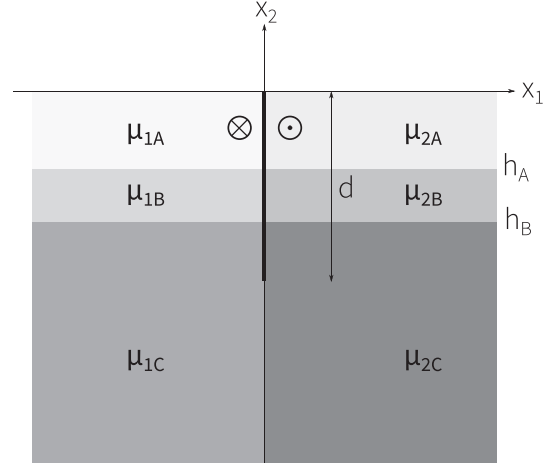
Figure A1. Superposition of dislocations in single-layered elastic structures to approximate the surface displacement of a similar dislocation in a multi-layered structure. In our examples, we choose $\mu_{1A}/\mu_{2C} = 0.3$, $\mu_{1B}/\mu_{2C} = 0.6$, $\mu_{2A}/\mu_{2C} = 0.44$, $\mu_{2B}/\mu_{2C} = 0.74$ and $\mu_{1C}/\mu_{2C} = 0.87$.

and K_B as

$$K_B = \frac{\mu_B - \mu_C}{\mu_B + \mu_C}.$$

(A7)

Each layer is thus characterized by a shear modulus expressed by:

$$\mu_1 = \frac{\mu_A + \mu_B}{2},$$
$$\mu_2 = \frac{\mu_B + \mu_C}{2},$$
$$\mu_3 = \mu_C$$

(A8)

A4 Strike-slip fault bounding two 2-layered media

Finally, we can investigate the case where a vertical strike-slip fault bounds two media, each characterized by two layers of different shear moduli overlying a half half-space (Fig. A1). As for the preceding examples, the two layers are of thickness h_A and h_B, the slip, s, extending from the free surface to a depth $d \geq h_B \geq h_A$.

We approximate the solution with a moduli perturbation approach (e.g. Du *et al.* 1994; Cervelli *et al.* 1999; Segall 2010). We assume that the surface displacement induced by a dislocation of slip s is equivalent to the superposition of three similar dislocations of slip s embedded in three different structure (2 with one horizontal layer, 1 with one vertical interface). Each layer (see Fig. A1) is characterized by a different shear modulus:

$$\mu_{1A} = \frac{1}{3}(\mu_1 + \mu_A + \mu_B),$$
$$\mu_{1B} = \frac{1}{3}(\mu_1 + \mu_B + \mu_C),$$
$$\mu_{1C} = \frac{1}{3}(\mu_1 + 2\mu_C),$$
$$\mu_{2A} = \frac{1}{3}(\mu_2 + \mu_A + \mu_B),$$
$$\mu_{2B} = \frac{1}{3}(\mu_2 + \mu_B + \mu_C),$$
$$\mu_{2C} = \frac{1}{3}(\mu_2 + 2\mu_C).$$

(A9)

The displacement induced at the free surface can be simply expressed as the sum of eqs (A.1) and (A.4):

$$u^{(1)}(x_1 < 0, x_2 = 0) = \frac{1}{3}\left[\frac{s}{\pi}\frac{\mu_2}{\mu_1 + \mu_2}\tan^{-1}\left(\frac{d}{x_1}\right)\right.$$
$$+ u_A(x_1 < 0, x_2 = 0)$$
$$\left. + u_B(x_1 < 0, x_2 = 0)\right], \tag{A10}$$

$$u^{(2)}(x_1 > 0, x_2 = 0) = \frac{1}{3}\left[\frac{s}{\pi}\frac{\mu_1}{\mu_1 + \mu_2}\tan^{-1}\left(\frac{d}{x_1}\right)\right.$$
$$+ u_A(x_1 > 0, x_2 = 0)$$
$$\left. + u_B(x_1 > 0, x_2 = 0)\right]. \tag{A11}$$

A5 Strike-slip fault embedded in a compliant fault zone

From Segall (2010), the expression of the surface displacement produced by an infinitely long vertical strike-slip fault embedded in a compliant fault zone of shear modulus μ_2, the remaining part of the half-space having a shear modulus of μ_1, is:

$$u_{dz}^{(1)}(x_1 < -h, x_2 = 0) = \frac{s(1-K)}{\pi}\sum_{m=0}^{+\infty} K^m \tan^{-1}\left(\frac{d}{x_1 - 2mh}\right)$$

$$u_{dz}^{(2)}(|x_1| < h, x_2 = 0) = \frac{s}{\pi}\tan^{-1}\left(\frac{d}{x_1}\right) +$$
$$\frac{s}{\pi}\sum_{m=1}^{+\infty} K^m\left[\tan^{-1}\left(\frac{d}{x_1 - 2mh}\right) + \tan^{-1}\left(\frac{d}{x_1 + 2mh}\right)\right]$$

$$u_{dz}^{(3)}(x_1 > h, x_2 = 0) = \frac{s(1-K)}{\pi}\sum_{m=0}^{+\infty} K^m \tan^{-1}\left(\frac{d}{x_1 + 2mh}\right). \tag{A12}$$

The slip, s, on the fault extends from the free surface to depth d, the thickness of the fault zone is $2h$, centred around $x_1 = 0$, and K is ($\mu_1 > \mu_2$):

$$K = \frac{\mu_1 - \mu_2}{\mu_1 + \mu_2}. \tag{A13}$$

APPENDIX B: EXPRESSIONS OF GREEN'S FUNCTIONS AND SENSITIVITY KERNELS FOR A STRIKE-SLIP DISLOCATION IN A 2.5-D MEDIUM

From the expressions of the surface displacement presented in the precedent section, we can derive the expression of the Green's functions and their derivatives. The Green's functions are the surface displacement induced by a unit slip on one subfault. We will consider a subfault f_i of width $\delta d = d_{i+1} - d_i$, $d_{i+1} \geq d_i$. The Green's function $G(x_j, f_i)$ can be expressed as the difference between the surface displacement due to a finite dislocation between the free surface and depth d_{i+1}, and another finite dislocation between the free surface and depth d_i.

B1 Strike-slip fault bounding two media

For an infinitely long vertical strike-slip fault bounding two media of different shear modulus, μ_1 and μ_2, we thus have, following eq. (A1):

$$\mathbf{G}_v^{(1)}(x_j, f_i) = u_v^{(1)}(x_j, d_{i+1}) - u_v^{(1)}(x_j, d_i)$$
$$\mathbf{G}_v^{(2)}(x_j, f_i) = u_v^{(2)}(x_j, d_{i+1}) - u_v^{(2)}(x_j, d_i) \tag{B1}$$

$$\mathbf{G}_v^{(1)}(x_j, f_i) = \frac{2}{\pi}\frac{\mu_2}{\mu_1 + \mu_2}\left[\tan^{-1}\left(\frac{d_{i+1}}{x_j}\right) - \tan^{-1}\left(\frac{d_i}{x_j}\right)\right]$$

$$\mathbf{G}_v^{(2)}(x_j, f_i) = \frac{2}{\pi}\frac{\mu_1}{\mu_1 + \mu_2}\left[\tan^{-1}\left(\frac{d_{i+1}}{x_j}\right) - \tan^{-1}\left(\frac{d_i}{x_j}\right)\right] \tag{B2}$$

We can then derive the expressions of the sensitivity kernels of the Green's functions with respect to each shear modulus. As the shear modulus, μ, is a Jeffrey's parameter (e.g. Tarantola 2005), the generic expression of the sensitivity kernels is:

$$\mathbf{K}_\mu(x_j, f_i) = \frac{\partial\, \mathbf{G}(x_j, f_i)}{\partial \ln \mu} = \frac{\partial\, \mathbf{G}(x_j, f_i)}{\partial \mu} \cdot \mu. \tag{B3}$$

We thus have:

$$\mathbf{K}_{v,\mu_1}^{(1)}(x_j, f_i) = -\frac{2}{\pi}\frac{\mu_2 \cdot \mu_1}{(\mu_1 + \mu_2)^2}\left[\tan^{-1}\left(\frac{d_{i+1}}{x_j}\right) - \tan^{-1}\left(\frac{d_i}{x_j}\right)\right]$$

$$\mathbf{K}_{v,\mu_1}^{(2)}(x_j, f_i) = \frac{2}{\pi}\frac{\mu_1^2}{(\mu_1 + \mu_2)^2}\left[\tan^{-1}\left(\frac{d_{i+1}}{x_j}\right) - \tan^{-1}\left(\frac{d_i}{x_j}\right)\right] \tag{B4}$$

$$\mathbf{K}_{v,\mu_2}^{(1)}(x_j, f_i) = \frac{2}{\pi}\frac{\mu_2^2}{(\mu_1 + \mu_2)^2}\left[\tan^{-1}\left(\frac{d_{i+1}}{x_j}\right) - \tan^{-1}\left(\frac{d_i}{x_j}\right)\right]$$

$$\mathbf{K}_{v,\mu_2}^{(2)}(x_j, f_i) = -\frac{2}{\pi}\frac{\mu_1 \cdot \mu_2}{(\mu_1 + \mu_2)^2}\left[\tan^{-1}\left(\frac{d_{i+1}}{x_j}\right) - \tan^{-1}\left(\frac{d_i}{x_j}\right)\right] \tag{B5}$$

B2 One layer above half-space

Similarly, we can also calculate the Green's functions for a strike-slip fault embedded in a medium composed of one horizontal layer of thickness h_A and shear modulus μ_A, overlying a half-space of different shear modulus μ_C.

If $d \geq h_A$, from eq. (A.2):

$$\mathbf{G}_1(x_j, f_i) = \frac{1 - K_A}{\pi}\left[\tan^{-1}\left(\frac{d_{i+1}}{x_j}\right) - \tan^{-1}\left(\frac{d_i}{x_j}\right)\right]$$
$$+ \frac{1 - K_A}{\pi}\sum_{m=1}^{+\infty} K_A^m\left[\tan^{-1}\left(\frac{d_{i+1} + 2mh_A}{x_j}\right)\right.$$
$$\left. - \tan^{-1}\left(\frac{d_i + 2mh_A}{x_j}\right)\right]. \tag{B6}$$

If $d \leq h_A$, from eq. (A.4):

$$\mathbf{G}_1(x_j, f_i) = \frac{1}{\pi}\left[\tan^{-1}\left(\frac{d_{i+1}}{x_j}\right) - \tan^{-1}\left(\frac{d_i}{x_j}\right)\right]$$
$$+ \frac{1}{\pi}\sum_{m=1}^{+\infty} K_A^m\left[\tan^{-1}\left(\frac{d_{i+1} + 2mh_A}{x_j}\right)\right.$$
$$+ \tan^{-1}\left(\frac{d_{i+1} - 2mh_A}{x_j}\right)$$
$$- \tan^{-1}\left(\frac{d_i + 2mh_A}{x_j}\right)$$
$$\left. - \tan^{-1}\left(\frac{d_i - 2mh_A}{x_j}\right)\right], \tag{B7}$$

We can then derive the expressions of the sensitivity kernels of the Green's functions with respect to μ_A:

If $d \geq h_A$,

$$\mathbf{K_{1,\mu_A}}(x_j, f_i) = -\frac{2}{\pi} \frac{\mu_C \cdot \mu_A}{(\mu_A + \mu_C)^2} \left[\tan^{-1}\left(\frac{d_{i+1}}{x_j}\right) - \tan^{-1}\left(\frac{d_i}{x_j}\right) \right]$$
$$- \frac{2}{\pi} \frac{\mu_C \cdot \mu_A}{(\mu_A + \mu_C)^2} \sum_{m=1}^{+\infty} K_A^m \left[\tan^{-1}\left(\frac{d_{i+1} + 2mh_A}{x_j}\right) \right.$$
$$\left. - \tan^{-1}\left(\frac{d_i + 2mh_A}{x_j}\right) \right]$$
$$- \frac{2}{\pi} \frac{(1 - K_A)\, \mu_C \cdot \mu_A}{(\mu_C - \mu_A)^2} \sum_{m=1}^{+\infty} m\, K_A^m \left[\tan^{-1}\left(\frac{d_{i+1} + 2mh_A}{x_j}\right) \right.$$
$$\left. - \tan^{-1}\left(\frac{d_i + 2mh_A}{x_j}\right) \right]. \tag{B8}$$

If $d \leq h_A$,

$$\mathbf{K_{1,\mu_A}}(x_j, f_i) = \frac{2}{\pi} \sum_{m=1}^{+\infty} \frac{m \cdot \mu_C \cdot \mu_A}{(\mu_C - \mu_A)^2} K_A^m \left[\tan^{-1}\left(\frac{d_{i+1} + 2mh_A}{x_j}\right) \right.$$
$$+ \tan^{-1}\left(\frac{d_{i+1} - 2mh_A}{x_j}\right)$$
$$- \tan^{-1}\left(\frac{d_i + 2mh_A}{x_j}\right)$$
$$\left. - \tan^{-1}\left(\frac{d_i - 2mh_A}{x_j}\right) \right]. \tag{B9}$$

And with respect to μ_C, if $d \geq h_A$:

$$\mathbf{K_{1,\mu_c}}(x_j, f_i) = \frac{2}{\pi} \frac{\mu_A \cdot \mu_C}{(\mu_A + \mu_C)^2} \left[\tan^{-1}\left(\frac{d_{i+1}}{x_j}\right) - \tan^{-1}\left(\frac{d_i}{x_j}\right) \right]$$
$$+ \frac{2}{\pi} \frac{\mu_A \cdot \mu_C}{(\mu_A + \mu_C)^2} \sum_{m=1}^{+\infty} K_A^m \left[\tan^{-1}\left(\frac{d_{i+1} + 2mh_A}{x_j}\right) \right.$$
$$\left. - \tan^{-1}\left(\frac{d_i + 2mh_A}{x_j}\right) \right]$$
$$- \frac{4}{\pi} \frac{\mu_A \cdot \mu_C^2}{(\mu_A + \mu_C)^3} \sum_{m=0}^{+\infty} (m + 1)\, K_A^m \left[\tan^{-1}\left(\frac{d_{i+1} + 2mh_A}{x_j}\right) \right.$$
$$\left. - \tan^{-1}\left(\frac{d_i + 2mh_A}{x_j}\right) \right]. \tag{B10}$$

If $d \leq h_A$:

$$\mathbf{K_{1,\mu_c}}(x_j, f_i) = -\frac{2}{\pi} \sum_{m=1}^{+\infty} \frac{m \cdot \mu_C \cdot \mu_A}{(\mu_A + \mu_C)^2} K_A^{m-1} \cdot$$
$$\left[\tan^{-1}\left(\frac{d_{i+1} + 2mh_A}{x_j}\right) \right.$$
$$+ \tan^{-1}\left(\frac{d_{i+1} - 2mh_A}{x_j}\right)$$
$$- \tan^{-1}\left(\frac{d_i + 2mh_A}{x_j}\right)$$
$$\left. - \tan^{-1}\left(\frac{d_i - 2mh_A}{x_j}\right) \right]. \tag{B11}$$

B3 Other structures

Similarly to the previous sections, we can derive the expressions of the Green's functions and sensitivity kernels for a compliant fault zone, or approximate them for more complex structures. We do not replicate these expressions as the derivatives are very similar to the ones presented in Section B2.

Key words

Authors are requested to choose key words from the list below to describe their work. The key words will be printed underneath the summary and are useful for readers and researchers. Key words should be separated by a semi-colon and listed in the order that they appear in this list. An article should contain no more than six key words.

COMPOSITION and PHYSICAL PROPERTIES
Composition and structure of the continental crust
Composition and structure of the core
Composition and structure of the mantle
Composition and structure of the oceanic crust
Composition of the planets
Creep and deformation
Defects
Elasticity and anelasticity
Electrical properties
Equations of state
Fault zone rheology
Fracture and flow
Friction
High-pressure behaviour
Magnetic properties
Microstructure
Permeability and porosity
Phase transitions
Plasticity, diffusion, and creep

GENERAL SUBJECTS
Core
Gas and hydrate systems
Geomechanics
Geomorphology
Glaciology
Heat flow
Hydrogeophysics
Hydrology
Hydrothermal systems
Infrasound
Instrumental noise
Ionosphere/atmosphere interactions
Ionosphere/magnetosphere interactions
Mantle processes
Ocean drilling
Structure of the Earth
Thermochronology
Tsunamis
Ultra-high pressure metamorphism
Ultra-high temperature metamorphism

GEODESY and GRAVITY
Acoustic-gravity waves
Earth rotation variations
Geodetic instrumentation
Geopotential theory
Global change from geodesy
Gravity anomalies and Earth structure
Loading of the Earth
Lunar and planetary geodesy and gravity
Plate motions
Radar interferometry
Reference systems
Satellite geodesy
Satellite gravity
Sea level change

Seismic cycle
Space geodetic surveys
Tides and planetary waves
Time variable gravity
Transient deformation

GEOGRAPHIC LOCATION
Africa
Antarctica
Arctic region
Asia
Atlantic Ocean
Australia
Europe
Indian Ocean
Japan
New Zealand
North America
Pacific Ocean
South America

GEOMAGNETISM and ELECTROMAGNETISM
Archaeomagnetism
Biogenic magnetic minerals
Controlled source electromagnetics (CSEM)
Dynamo: theories and simulations
Electrical anisotropy
Electrical resistivity tomography (ERT)
Electromagnetic theory
Environmental magnetism
Geomagnetic excursions
Geomagnetic induction
Ground penetrating radar
Magnetic anomalies: modelling and
    interpretation
Magnetic fabrics and anisotropy
Magnetic field variations through time
Magnetic mineralogy and petrology
Magnetostratigraphy
Magnetotellurics
Marine electromagnetics
Marine magnetics and palaeomagnetics
Non-linear electromagnetics
Palaeointensity
Palaeomagnetic secular variation
Palaeomagnetism
Rapid time variations
Remagnetization
Reversals: process, time scale,
    magnetostratigraphy
Rock and mineral magnetism
Satellite magnetics

GEOPHYSICAL METHODS
Downhole methods
Fourier analysis
Fractals and multifractals
Image processing

Instability analysis
Interferometry
Inverse theory
Joint inversion
Neural networks, fuzzy logic
Non-linear differential equations
Numerical approximations and analysis
Numerical modelling
Numerical solutions
Persistence, memory, correlations, clustering
Probabilistic forecasting
Probability distributions
Self-organization
Spatial analysis
Statistical methods
Thermobarometry
Time-series analysis
Tomography
Waveform inversion
Wavelet transform

PLANETS
Planetary interiors
Planetary volcanism

SEISMOLOGY
Acoustic properties
Body waves
Coda waves
Computational seismology
Controlled source seismology
Crustal imaging
Earthquake dynamics
Earthquake early warning
Earthquake ground motions
Earthquake hazards
Earthquake interaction, forecasting,
    and prediction
Earthquake monitoring and test-ban
    treaty verification
Earthquake source observations
Guided waves
Induced seismicity
Interface waves
Palaeoseismology
Rheology and friction of fault zones
Rotational seismology
Seismic anisotropy
Seismic attenuation
Seismic instruments
Seismic interferometry
Seismicity and tectonics
Seismic noise
Seismic tomography
Site effects
Statistical seismology
Surface waves and free oscillations
Theoretical seismology

Tsunami warning
Volcano seismology
Wave propagation
Wave scattering and diffraction

TECTONOPHYSICS
Backarc basin processes
Continental margins: convergent
Continental margins: divergent
Continental margins: transform
Continental neotectonics
Continental tectonics: compressional
Continental tectonics: extensional
Continental tectonics: strike-slip and transform
Cratons
Crustal structure
Diapirism
Dynamics: convection currents, and mantle
   plumes
Dynamics: gravity and tectonics
Dynamics: seismotectonics
Dynamics and mechanics of faulting
Dynamics of lithosphere and mantle
Folds and folding
Fractures, faults, and high strain
   deformation zones
Heat generation and transport

Hotspots
Impact phenomena
Intra-plate processes
Kinematics of crustal and mantle deformation
Large igneous provinces
Lithospheric flexure
Mechanics, theory, and modelling
Microstructures
Mid-ocean ridge processes
Neotectonics
Obduction tectonics
Oceanic hotspots and intraplate volcanism
Oceanic plateaus and microcontinents
Oceanic transform and fracture zone processes
Paleoseismology
Planetary tectonics
Rheology: crust and lithosphere
Rheology: mantle
Rheology and friction of fault zones
Sedimentary basin processes
Subduction zone processes
Submarine landslides
Submarine tectonics and volcanism
Tectonics and climatic interactions
Tectonics and landscape evolution
Transform faults
Volcanic arc processes

VOLCANOLOGY
Atmospheric effects (volcano)
Calderas
Effusive volcanism
Eruption mechanisms and flow emplacement
Experimental volcanism
Explosive volcanism
Lava rheology and morphology
Magma chamber processes
Magma genesis and partial melting
Magma migration and fragmentation
Mud volcanism
Physics and chemistry of magma bodies
Physics of magma and magma bodies
Planetary volcanism
Pluton emplacement
Remote sensing of volcanoes
Subaqueous volcanism
Tephrochronology
Volcanic gases
Volcanic hazards and risks
Volcaniclastic deposits
Volcano/climate interactions
Volcano monitoring
Volcano seismology